Development of A Fast Radiative Transfer Model for Ground-based Microwave Radiometers (ARMS-gb v1.0): Validation and Comparison to RTTOV-gb

Yi-Ning Shi[1,2], Jun Yang[1,2], Wei Han[1,2], Lujie Han[3,4], Jiajia Mao[3], Wanlin Kan[5,1], and Fuzhong Weng[1,2]

[1]State Key Laboratory of Severe Weather, Chinese Academy of Meteorological Sciences, China Meteorological Administration, Beijing 100081
[2]CMA Earth System Modeling and Prediction Centre, China Meteorological Administration, Beijing 100081
[3]Meteorological Observation Center of CMA, China Meteorological Administration, Beijing 100081
[4]Zhejiang Lin'an Atmospheric Background National Observation and Research Station, Hangzhou 311300
[5]Key Laboratory of Transportation Meteorology of China Meteorological Administration, Nanjing Joint Institute for Atmospheric Sciences, Nanjing 210041

Correspondence: Jun Yang (yangjun@cma.gov.cn)

Abstract. ~~A~~ This study proposes a fast radiative transfer model~~(RTM)~~, ARMS-gb, ~~capable of simulating~~ designed to simulate brightness temperatures observed by ground-based microwave radiometers (GMRs)~~is proposed in this study. Several improvements are introduced in the Optical Depth in Pressure Space scheme to achieve higher accuracy. 101-level ECMWF 83 profiles are utilized as its primary training dataset. Seven additional profiles from UMBC 48 are augmented with this dataset to improve simulation accuracy~~. ARMS-gb employs a clear-sky radiative transfer (RT) solver to account for atmospheric thermal emissions, while gaseous absorption is estimated using a statistical regression scheme. To enhance simulation accuracy, particularly in moist environments~~. When compared to MonoRTM, ARMS-gb shows high accuracy with root mean square error less than 0.12 K for all observed channels of MP3000A and HATPRO. An~~ , seven humid profiles from the University of Maryland at Baltimore County 48-profile dataset are added to the European Centre for Medium-Range Weather Forecasts 83-profile dataset to train the gaseous absorption scheme. Additionally, an advanced water vapor vertical interpolation ~~mode is also incorporated, which generally proves more accurate than that~~ method is incorporated, offering improved accuracy compared to the interpolation method used in RTTOV-gb. ~~Bias drops can reach up to 0.19 K for mean biases (AVG) and~~ The standard deviation is reduced by 0.15 K ~~for standard deviation (STD)~~ in channels with strong water vapor absorption. Jacobian calculated by these two interpolation modes are also ~~differ~~different. To further validate ~~the performance of~~ ARMS-gb~~, it is applied in simulating real observations from GMRs, with the simulated results compared to those of~~ 's performance, simulations using both ARMS-gb and RTTOV-gb ~~. Long-term~~ are compared against real observations from two GMRs~~under different climate conditions are selected as true reference values. Results show~~ . The Observation Minus Background analyses demonstrate that ARMS-gb ~~align~~ aligns well with RTTOV-gb ~~well and can achieve smaller STD in water vapor absorption channels~~and achieves smaller STDs under high-humidity conditions. Furthermore, the ~~calibration time is more clearly identified in the observations minus background series~~ ability of ARMS-gb ~~compared to original observation series, demonstrating its ability to monitor observational quality~~to monitor GMRs' observational quality is demonstrated.

1 Introduction

Ground-based microwave radiometers (GMRs) are considered vital tools in meteorological research due to their ability to provide continuous, high-temporal-resolution observations of atmospheric ~~thermal~~ thermodynamical variables (Cimini et al., 2006; Wei et al., 2021). These instruments can operate under all-sky conditions, making them particularly useful for monitoring rapid changes within the planetary boundary layer (PBL). The PBL, which ~~extends~~ may extend from the surface to a few kilometers above, is a critical region where exchanges of heat, moisture, and momentum between the ground and the atmosphere predominantly occur (Wu et al., 2024). Observations from GMRs offer a unique advantage for understanding PBL dynamics, providing valuable insights into processes such as convection, turbulence, and boundary layer transitions (De Angelis et al., 2017).

The assimilation of GMR observations into Numerical Weather Prediction (NWP) models holds significant potential for enhancing forecast accuracy, particularly in the lower atmosphere. Current NWP models often face substantial uncertainties near the ground surface due to both observational gaps and the complex physical processes within the PBL. By incorporating GMR observations, temperature and humidity in the PBL can be more accurately characterized, leading to improved initial conditions for NWP models (Illingworth et al., 2019; Leuenberger et al., 2020). Consequently, temperature and humidity profiles retrieved from GMR observations have been assimilated into NWPs in previous studies (e.g., Caumont et al., 2016; Martinet et al., 2020). These studies show that such indirect assimilations enhance the accuracy of forecasts involving temperature inversions and humidity gradients, which are crucial for predicting fog and the initiation of convection. However, the performance of these assimilations is often limited by challenges in estimating biases in GMR observations (Lin et al., 2023). This limitation can be mitigated by directly assimilating the observed brightness temperatures (BTs) from GMRs. Vural et al. (2024) demonstrated a positive impact on forecasting temperature and humidity in the PBL by directly assimilating BTs from two channels. The advantage of direct assimilation of GMR observations is further highlighted when compared to indirect assimilation results in forecasting extreme precipitation events (Cao et al., 2023). Radiative transfer models (RTMs) are essential in direct data assimilation, as they map atmospheric parameters from NWP models into satellite or GMR observations. Numerous fast RTMs have been developed for the direct assimilation of satellite observations, such as the Radiative Transfer for TOVS (RTTOV) (Saunders et al., 2018; Hocking et al., 2021), the Community Radiative Transfer Model (CRTM) (Weng and Liu, 2003; Stegmann et al., 2022; Karpowicz et al., 2022), and the Advanced Radiative Transfer Modeling System (ARMS) (Weng et al., 2020; Yang et al., 2020). For use with GMRs, few RTMs are specifically designed for this purpose, with RTTOV-ground-based (RTTOV-gb) (De Angelis et al., 2016; Cimini et al., 2019) being a notable exception. Unlike the traditional RTTOV, RTTOV-gb is optimized to handle the unique geometries and atmospheric paths associated with GMRs. ~~RTTOV-gb is~~ While the coefficients for RTTOV are trained using AMSUTRAN (Turner et al., 2019), ~~which itself is based on~~ the coefficients for RTTOV-gb are trained using an updated version of the Millimeter-wave Propagation Model~~(MPM)(Liebe, 1985, 1989; Liebe et al., 1992, 1993)~~, as detailed by Rosenkranz (1998) (hereafter referred to as R98). A further updated version of R98 is introduced by Rosenkranz (2017) (hereafter referred to as R17), and its uncertainties are analyzed by Cimini et al. (2018). RTTOV-gb v1.0, now supports both coefficients trained using the R98 and R17.

In addition to AMSUTRAN, R98 and R17, the Monochromatic Radiative Transfer Model (MonoRTM) can also provide Line-By-Line (LBL) results of radiance and transmittance, and its accuracy in simulating upwelling radiative transfer (RT) has been evaluated against AMSUTRAN (Cady-Pereira et al., 2021). On the other hand, for downwelling RT simulations, BTs produced by different types of LBL models can vary significantly. A study comparing results from five different LBL models found discrepancies as large as 1.5 K in channel 1 of the MP3000A (Yang and Min, 2018), underscoring the importance of using a reliable and accurate LBL model to train fast RTMs for optimal performance. However, there are few studies that provide intercomparisons between fast RTMs trained with different microwave LBL models in downwelling RT simulations.

Furthermore, due to the use of terrain-following coordinates, the pressure levels in NWP models are not fixed, necessitating vertical interpolation in both RTTOV and RTTOV-gb. Hocking (2014) compared five vertical interpolation methods within RTTOV, finding that the choice of interpolation mode affects not only the simulated BTs but also the Jacobian calculations. Kan et al. (2024) proposed an advanced water vapor interpolation method, significantly reducing biases caused by vertical interpolation in water vapor absorption channels of microwave sensors onboard satellites. It is important to evaluate the differences in forward simulations and Jacobians caused by vertical interpolation modes from the perspective of GMR applications.

In this study, a new RTM (ARMS-gb) capable of simulating BTs observed by GMRs and their Jacobian is proposed. ARMS-gb relies on a clear-sky RT solver and employs MonoRTM to train the gaseous absorption scheme. The accuracy of ARMS-gb in moist environment is improved by ~~expanding~~ enriching the training dataset and incorporating the advanced interpolation mode proposed by Kan et al. (2024). This development also marks the first intercomparison between two fast RTMs for GMRs. In the following section, each ~~components~~ component of ARMS-gb ~~are introduced~~ is described in detail, including ~~a~~ the clear-sky ~~RT~~ radiative transfer (RT) solver, the gaseous absorption scheme~~and a~~ , and the Jacobian calculation module. ~~In section~~ Section 3 ~~,~~ investigates the accuracy of ARMS-gb ~~is investigated~~ by comparing its results ~~to that~~ with those of MonoRTM. The improvements in accuracy achieved by enriching the training dataset are evaluated, and the impact of vertical interpolation on both forward simulations and Jacobian calculations is ~~also~~ analyzed. In ~~section~~ Section 4, ~~we compare simulating results between~~ ARMS-gb and RTTOV-gb ~~. Observations~~ are used to simulate real observations from two GMRs under different climate conditions~~are used as true reference values. The ability~~ . Observation Minus Background (OMB) analyses from the two RTMs are compared. Additionally, the capability of ARMS-gb to monitor ~~GMRs' observational quality is also~~ the observational quality of GMRs is demonstrated. A summary ~~is given in section~~ of the findings is provided in Section 5.

2 Model Development

The primary objective of this study is to develop ARMS-gb capable of simulating BTs observed by GMRs. These BTs are directly linked to downwelling radiances at the surface. Currently, ARMS-gb is limited to simulations under clear-sky conditions; however, a particle scattering module will be integrated in the near future to extend its capabilities and enable simulations under all-sky conditions.

2.1 Clear-sky RT equation

Without considering scattering effect, the RT equation (Liou, 1992) simplifies to

$$\mu \frac{dI(\tau,\mu)}{d\tau} = I(\tau,\mu) - B(\tau), \tag{1}$$

where $I(\tau,\mu)$ represents the radiance. τ and μ are the optical depth in the vertical direction and the cosine of the viewing zenith angle. A vertical measurement by a GMR corresponds to a zenith angle of $0°$. The vertical distribution of the Planck function $B(\tau)$ is described by the linear-in-tau approximation (Toon et al., 1989; Zhang et al., 2016, 2018) in ARMS-gb as

$$B(\tau) = B_0(1 + \beta\tau), \tag{2}$$

where $\beta = (B_1/B_0 - 1)/\tau_0$. B_0 and B_1 are the Planck functions at the upper and lower boundaries of the atmospheric layer, respectively. τ_0 is vertical optical depth of the atmospheric layer. After substituting Eq. (2) into Eq. (1) and solving Eq. (1), we can get

$$I(\tau_0,\mu) = I(0,\mu)e^{-d} + B_1 - B_0 e^{-d} - \frac{(1-e^{-d})}{d}(B_1 - B_0), \tag{3}$$

where $d = \tau_0/\mu$. $I(0,\mu)$ and $I(\tau_0,\mu)$ are the downwelling radiances at the upper and lower boundaries of the layer, respectively. In a multi-layer case, $I(0,\mu)$ can be obtained from results of the previous layer and $I(\tau_0,\mu)$ will serve as the boundary input for the next layer (Li and Fu, 2000; Zhang et al., 2017). Therefore, downwelling radiance is calculated layer by layer from the Top Of the Atmosphere (TOA) to the ground surface. The boundary input at TOA equals the cosmic background radiance.

2.2 Gaseous Absorption

The accuracy of d in Eq.(3), which represents the effect of gaseous absorption at the GMR observed frequency, is critical for the performance of RT simulations. To address this issue, we employ Optical Depth in Pressure Space (ODPS) (Saunders et al., 1999; Chen et al., 2010; Hocking et al., 2021), a statistical regression scheme. ODPS involves two stages: training and simulation processes. Recent improvements to both stages have been proposed by Kan et al. (2024) and assessed by comparing their results to satellite observations. Most of these enhancements have been incorporated into ARMS-gb.

The ODPS training process ~~utilizes ECMWF83 profiles as its primary~~ primarily uses the the European Centre for Medium-Range Weather Forecasts (ECMWF) 83-profile dataset. To ~~improve~~ enhance simulation accuracy, particularly in moist environments, ~~we augment this dataset~~ this dataset is augmented with seven additional profiles (1st, 6th, 14th, 15th, 16th, 18th, and 20th) from the University of Maryland at Baltimore County (UMBC) ~~48 profiles. MonoRTM Clough et al. (2005)~~ 48-profile dataset. Fig. 1 presents statistical comparisons of the water vapor profiles from the ECMWF 83-profile dataset and the seven additional profiles from the UMBC 48-profile dataset. The maximum, mean, minimum values, and standard deviation of the ECMWF 83-profile dataset are displayed, along with the humidity range of the additional profiles. The humidity range of the additional profiles exceeds the mean values plus the standard deviation of the ECMWF 83-profile dataset, particularly in the lower levels of the troposphere. Furthermore, the upper bound for optical depth regression is extended. The impact of this augmentation on simulation accuracy is discussed in Section 3.

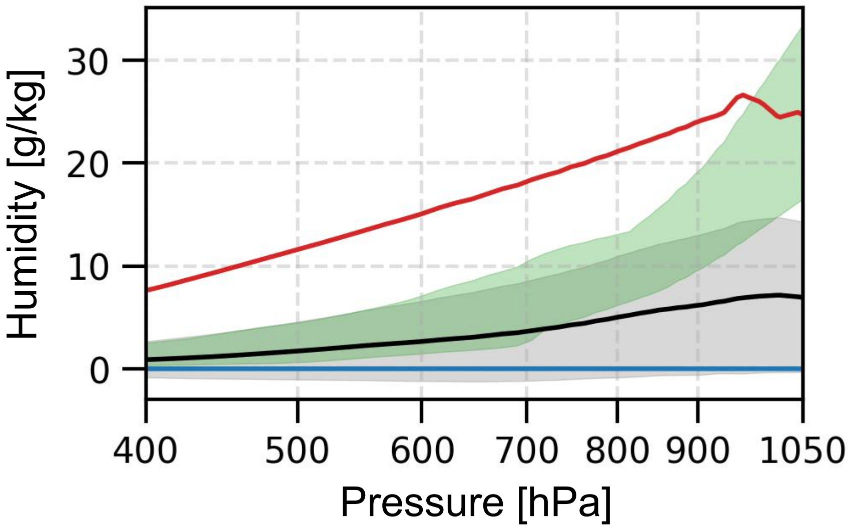

Figure 1. Statistical comparisons of the water vapor profiles from the ECMWF 83-profile dataset and the seven additional profiles from the UMBC 48-profile dataset. The red, black and blue lines represent the maximum, mean and minimum values of the ECMWF 83-profile dataset, respectively. The gray shaded area indicates the range within twice the standard deviation of the ECMWF 83-profile dataset. The green shaded area represents the range bounded by the maximum and minimum values of the seven additional profiles from the UMBC 48-profile dataset.

MonoRTM (Clough et al., 2005) is employed to calculate LBL transmittance at 7 observed zenith angles (0°, 36°, 48°, 55°, 60°, 63°, 70°). Water vapor absorption, oxygen absorption, ozone line absorption and nitrogen continuum absorption are considered. In MonoRTM, line absorption calculation relies on HITRAN database (Gordon et al., 2022) and continuum absorption is handled by the MT_CKD continuum model (Mlawer et al., 2012; Clough et al., 2005). As channel-dependent Spectral Response Functions (SRF) are not available, the transmittance of GMRs' channels is calculated as the mean of the monochromatic transmittance ~~in channel spectral~~ across the channel bandwidth V:

$$\Gamma_{\mathrm{ch},j} = \frac{\int_V \Gamma_j(v)dv}{\int_V dv}, \tag{4}$$

where the subscript j refers to the transmittance from the surface to the j-th level. $\Gamma_{\mathrm{ch},j}$ is the transmittance of an observed channel and $\Gamma_j(v)$ is the monochromatic transmittance. In practice, the channel bandwidth V is divided into 256 intervals and the integral in Eq. (4) is approximated by a discrete sum.

In ARMS-gb, water vapor is the only variable gas, while other gases are fixed during the training process. As a result, the total transmittance can be written as

$$\Gamma_{\mathrm{ch},j}^{\mathrm{total}} = \frac{\Gamma_{\mathrm{ch},j}^{\mathrm{total}}}{\Gamma_{\mathrm{ch},j}^{\mathrm{mixed}}} \Gamma_{\mathrm{ch},j}^{\mathrm{mixed}}, \tag{5}$$

where $\Gamma_{\mathrm{ch},j}^{\mathrm{total}}$ and $\Gamma_{\mathrm{ch},j}^{\mathrm{mixed}}$ are the total transmittance and the transmittance of all fixed gases, respectively. Following McMillin et al. (1995), We define the effective transmittance of water vapor $\Gamma_{\mathrm{ch},j}^{\mathrm{H_2O},*}$ as

$$\Gamma_{\mathrm{ch},j}^{\mathrm{H_2O},*} = \frac{\Gamma_{\mathrm{ch},j}^{\mathrm{total}}}{\Gamma_{\mathrm{ch},j}^{\mathrm{mixed}}}. \tag{6}$$

Both the water vapor absorption and overlap absorption are included in $\Gamma_{\mathrm{ch},j}^{\mathrm{H_2O},*}$. A linear regression is applied to fit layer optical depth related to $\Gamma_{\mathrm{ch},j}^{\mathrm{mixed}}$ and $\Gamma_{\mathrm{ch},j}^{\mathrm{H_2O},*}$:

$$d_j = D_j - D_{j+1} = \sum_{i=1}^{N_p} C_{i,j} X_{i,j}, \tag{7}$$

where d_j is the layer optical depth of the j-th layer which is bounded by the j-th level and the $(j+1)$-th level. $D_j = -\ln(\Gamma_{\mathrm{ch},j})$ is the optical depth from the surface to the j-th level. $X_{i,j}$ and $C_{i,j}$ are predictors and corresponding fitting coefficients, respectively. To achieve high accuracy, we construct a predictor pool first and then use the backward stepwise regression to select the optimal combination of predictors. The detailed information about the predictor pool can be found in Appendix A. Both the transmittance calculation and linear regression are performed at fixed 101 pressure levels. These pressure levels are identical to those used in RTTOV-gb (Angelis et al., 2016), which are ~~dense~~ denser below 2 km.

Most of NWP and reanalysis data have their own vertical coordinates whereas optical depth calculations are constrained to the 101 levels. Consequently, in the ODPS simulation process, temperatures and water vapors from input pressure levels are remapped onto the 101 levels using the Rochon interpolation (Rochon et al., 2007) for the purpose of calculating predictors. After the optical depth calculations, the resulting D_j values are interpolated back to the original input pressure levels via a nearest-neighbour log-linear interpolation.

GMRs are sensitive to atmospheric parameters near the surface. To improve simulation accuracy, temperatures and water vapor values at a height of 2 meters above ground level are used to correct the predictor values of the first layer above the surface. Furthermore, Kan et al. (2024) has shown that the logarithm of partial pressure is more effective than mass or volume mixing ratios in describing the vertical distribution of water vapor. In line with this finding, the unit of water vapor is converted to partial pressure, followed by a vertical interpolation of the logarithm of water vapor partial pressure to the 101 levels. The impact of this vertical interpolation on both forward simulation and Jacobian calculation is discussed in section 3.

2.3 Jacobian Calculation

Jacobian calculation is a crucial component of a ~~RT model~~RTM. It is essential for inversion and data assimilation.The aim of this calculation is to construct a K matrix that quantifies the sensitivity of radiances or BTs at each channel with respect to all input parameters. K matrix can be represented as:

$$\boldsymbol{K} = \begin{bmatrix} \partial I_1/\partial x_1 & \partial I_2/\partial x_1 & ... & \partial I_N/\partial x_1 \\ \partial I_1/\partial x_2 & \partial I_2/\partial x_2 & ... & \partial I_N/\partial x_2 \\ ... & ... & ... & ... \\ \partial I_1/\partial x_M & \partial I_2/\partial x_M & ... & \partial I_N/\partial x_M \end{bmatrix}, \tag{8}$$

where N and M denote the number of channels and input parameters, respectively. For RT simulations, N is generally much less than M. ~~There are three methods to obtain~~ In four-dimensional variational data assimilation systems, the K matrix ~~: the finite difference method,~~ is handled by the tangent linear ~~method~~ module and the adjoint ~~method (Errico, 1997). In the finite difference method, the derivative can be computed by perturbing a single input parameter:~~

$$\frac{\partial \boldsymbol{I}}{\partial x_j} = \frac{\boldsymbol{I}(x_j + \delta x) - \boldsymbol{I}(x_j)}{\delta x},$$

~~where $\boldsymbol{I} = \begin{bmatrix} I_1 & I_2 & \dots & I_N \end{bmatrix}$ represents the vector of radiance values at each channel. δx is a perturbation term. By repeating RT simulations M times and perturbing each input parameters , the K matrix can be calculated. The tangent linear module~~ module (Errico, 1997). The tangent linear module computes how small changes in the input parameters affect the RTM output. It is developed by ~~computing~~ deriving the derivatives for each step in the ~~RT model. The K matrix is deduced through the chain rule~~RTM. For example, in RT simulations, an input parameter x_j contribute to the radiance vector $\boldsymbol{I}$ alone the path:

$$x_j \rightarrow \boldsymbol{d} \rightarrow \boldsymbol{I}, \tag{9}$$

where $\boldsymbol{d}$ and $\boldsymbol{I}$ represent the vector of optical depth and radiance at each channel. Correspondingly, the tangent linear module can be expressed as

$$x_{\mathrm{TL,j}} \rightarrow \frac{\partial \boldsymbol{d}}{\partial x_j} \cdot x_{\mathrm{TL,j}} \rightarrow \frac{\partial \boldsymbol{I}}{\partial \boldsymbol{d}} \cdot \frac{\partial \boldsymbol{d}}{\partial x_j} \cdot x_{\mathrm{TL,j}}. \tag{10}$$

~~To obtain the K matrix,~~ The adjoint module is the backward counterpart of the tangent linear module~~also must be repeated M times. In contrast to the finite difference method, the tangent linear method provides analytical results. The adjoint method further improves computational efficiency by reversing the order of calculations within the tangent linear module:~~. It computes how small changes in the RTM output affect the input parameters. This process is represented as:

$$I_{\mathrm{AD,i}} \rightarrow \frac{\partial I_i}{\partial \boldsymbol{d}} \cdot I_{\mathrm{AD,i}} \rightarrow \frac{\partial I_i}{\partial \boldsymbol{d}} \cdot \frac{\partial \boldsymbol{d}}{\partial \boldsymbol{x}} \cdot I_{\mathrm{AD,i}}. \tag{11}$$

where $\boldsymbol{x} = \begin{bmatrix} x_1 & x_2 & \dots & x_M \end{bmatrix}$ is a vector containing all input parameters. ~~The adjoint method only requires repeating this process N times to calculate the K matrix.~~ In practice, ~~we first develop~~ the tangent linear module ~~and then derive~~ is developed first, and the adjoint module is subsequently derived from it.

The tangent linear and the adjoint modules work together to update the initial state of NWP based on observational data in four-dimensional variational data assimilation systems. The tangent linear module is used to evaluate how perturbations in the state evolve, while the adjoint model determines how these perturbations should be adjusted to minimize the difference between the RTM output and the actual observations.

3 Accuracy Evaluation of ARMS-gb

In this section, we ~~investigate~~ evaluate the accuracy of ARMS-gb by comparing its results to ~~that of MonoRTM . We also~~ those of MonoRTM and demonstrate the improvements achieved by enriching the training dataset. Additionally, we analyze the impact of vertical interpolation on both forward simulations and Jacobian calculations. ~~The evaluations are conducted~~ These evaluations are performed using two datasets: the ECMWF ~~83~~ 83-profile dataset and the UMBC ~~48~~ 48-profile dataset. Our analysis includes results at seven observed zenith angles: 0°, 36°, 48°, 55°, 60°, 63°, 70°. ARMS-gb currently supports two types of GMRs: the Humidity And Temperature PROfiler (HATPRO) and the MP3000A. The HATPRO, developed by Radiometer Physics GmbH, has 7 K-band channels (channels 1-7) and 7 V-band channels (channels 8-14). The center frequencies for each channel of the HATPRO are listed in Table 1. The MP3000A, designed by Radiometrics, provides observations at 22 distinct channels. The center frequencies for each channel of the MP3000A are presented in Table 2. Regarding bandwidths, the HATPRO has different values for its channels: 230 MHz for channels 1-11, 600 MHz for channel 12, 1000 MHz for channel 13, and 2000 MHz for channel 14. In contrast, all channels of the MP3000A have a uniform bandwidth of 300 MHz.

Table 1. Center frequencies of HATPRO.

Channel	1	2	3	4	5	6	7
Frequency (GHz)	22.24	23.04	23.84	25.44	26.24	27.84	31.04
Channel	8	9	10	11	12	13	14
Frequency (GHz)	51.26	52.28	53.86	54.94	56.66	57.30	58.00

Table 2. Center frequencies of MP3000A.

Channel	1	2	3	4	5	6	7	8
Frequency (GHz)	22.234	22.500	23.034	23.834	25.000	26.234	28.000	30.000
Channel	9	10	11	12	13	14	15	16
Frequency (GHz)	51.248	51.760	52.280	52.804	53.336	53.848	54.400	54.940
Channel	17	18	19	20	21	22		
Frequency (GHz)	55.500	56.020	56.660	57.288	57.964	58.800		

To evaluate the accuracy of ARMS-gb, we use three metrics: mean bias (AVG), standard deviation (STD) and root mean square error (RMS). These metrics are calculated as follows:

$$\mathrm{AVG} = \cancel{\frac{\sum_{i=1}^{N}[\mathrm{BT_{ben}}(i)-\mathrm{BT_{sim}}(i)]}{N}} \frac{\sum_{i=1}^{N_S}[\mathrm{BT_{ben}}(i)-\mathrm{BT_{sim}}(i)]}{N_S}, \tag{12}$$

$$\mathrm{STD} = \cancel{\sqrt{\frac{\sum_{i=1}^{N}[\mathrm{BT_{ben}}(i)-\mathrm{BT_{sim}}(i)-\mathrm{AVG}]^2}{N}}} \sqrt{\frac{\sum_{i=1}^{N_S}[\mathrm{BT_{ben}}(i)-\mathrm{BT_{sim}}(i)-\mathrm{AVG}]^2}{N_S}}, \tag{13}$$

$$\mathrm{RMS} = \cancel{\sqrt{\frac{\sum_{i=1}^{N}[\mathrm{BT_{ben}}(i)-\mathrm{BT_{sim}}(i)]^2}{N}}} \sqrt{\frac{\sum_{i=1}^{N_S}[\mathrm{BT_{ben}}(i)-\mathrm{BT_{sim}}(i)]^2}{N_S}}, \tag{14}$$

where ~~N~~ N_S is the total number of samples. $\mathrm{BT_{ben}}$ are the benchmark values of BTs and $\mathrm{BT_{sim}}$ are simulated BTs. The benchmark values are calculated using MonoRTM ~~as follows~~through the following steps: (1) Calculate ~~monochromatic radiance~~the monochromatic radiance $I(v)$; (2) Integrate the monochromatic radiance over the channel ~~spectral range~~ bandwidth V to obtain the channel-averaged radiance:

$$I_{\mathrm{ch}} = \frac{\int_V I(v)dv}{\int_V dv}. \tag{15}$$

where ~~$I(v)$ is the monochromatic radiance and~~ I_{ch} is the channel-averaged radiance. Similar to Eq. (4), the integral calculation in Eq. (16) is also discretised as a sum, with the channel bandwidth V divided into 256 intervals prior to summation.

~~(a): AVGs, STDs and RMSs of simulated BTs at 7 observed zenith angles in MP3000A channels under the 101L ECMWF 83 dataset. Results of MonoRTM serve as the benchmark values. (b): Same as (a) but RT simulations are performed under the 101L UMBC 48 dataset. (c) and (d): Same as (a) and (b), but show the situations in HATPRO channels.~~

3.1 Effect of enriching the training dataset

~~Fig.~~

To evaluate the impact of enriching the training dataset, we trained two sets of fitting coefficients: one using the ECMWF 83-profile dataset (hereafter referred to as Coef_EC83) and the other using the new training dataset (hereafter referred to as Coef_New90). RT simulations based on these two coefficients are intercompared using the 101-level ~~(a) shows~~ 101L) ECMWF 83-profile and UMBC 48-profile dataset. The 101 pressure levels are specifically chosen to eliminate effects related to vertical interpolation. AVG, STD and RMS ~~of each channel of MP3000A under~~ for each HATPRO channel are presented in Table 3. For the 101L ECMWF ~~83 dataset. The results show high accuracyfor ARMS-gb in this case, with RMS values less than 0.12~~83-profile dataset, the accuracy of the two fitting coefficients is comparable, with the maximum RMS difference between them being only 0.0078 K. Both coefficients achieve high accuracy: in channels 1–7 and 10, the RMS is approximately 0.03 K, while in channels 11–14, the RMS is less than 0.012 K~~for all observed channels. Notably, biases for channels between~~ . However, biases are slightly larger in channels within the 51~~GHz and~~ –54 GHz ~~are larger than those for other channels, with a maximum RMS of 0.11~~range, with the maximum RMS exceeding 0.1 K ~~at~~ in channel 9. This larger bias is attributed to the

Table 3. AVG, STD and RMS of each channel of HATPRO. RT simulations based on Coef_EC83 and Coef_New90 are performed under the 101L ECMWF 83-profile and UMBC 48-profile dataset. MonoRTM serves as a benchmark to provide reference values for the comparison.

101L ECMWF 83-profile dataset								
Coefs	Channel	1	2	3	4	5	6	7
Coef_EC83	AVG (K)	0.0188	0.0139	0.0157	0.0167	0.0185	0.0194	0.0200
Coef_New90	AVG (K)	0.0156	0.0123	0.0115	0.0150	0.0164	0.0186	0.0190
Coef_EC83	STD (K)	0.0341	0.0316	0.0262	0.0251	0.0251	0.0266	0.0322
Coef_New90	STD (K)	0.0366	0.0341	0.0290	0.0263	0.0261	0.0274	0.0334
Coef_EC83	RMS (K)	0.0389	0.0345	0.0305	0.0301	0.0312	0.0329	0.0379
Coef_New90	RMS (K)	0.0389	0.0362	0.0312	0.0302	0.0308	0.0332	0.0384
Coefs	Channel	8	9	10	11	12	13	14
Coef_EC83	AVG (K)	0.0121	0.0176	-0.0001	0.0007	0.0001	0.0007	0.0010
Coef_New90	AVG (K)	0.0118	0.0042	0.0011	0.0006	0.0008	0.0006	0.0011
Coef_EC83	STD (K)	0.1018	0.0937	0.0385	0.0111	0.0037	0.0030	0.0027
Coef_New90	STD (K)	0.1097	0.0989	0.0393	0.0109	0.0039	0.0030	0.0028
Coef_EC83	RMS (K)	0.1025	0.0954	0.0385	0.0111	0.0037	0.0031	0.0028
Coef_New90	RMS (K)	0.1103	0.0990	0.0393	0.0109	0.0040	0.0031	0.0031
101L UMBC 48-profile dataset								
Coefs	Channel	1	2	3	4	5	6	7
Coef_EC83	AVG (K)	-1.1162	0.0630	-0.0737	-1.0613	-0.4619	0.1545	-0.5697
Coef_New90	AVG (K)	0.0430	0.0378	0.0327	0.0322	0.0298	0.0303	0.0300
Coef_EC83	STD (K)	3.6620	0.1940	0.1666	2.6362	0.5401	0.4241	0.6797
Coef_New90	STD (K)	0.0439	0.0329	0.0234	0.0207	0.0208	0.0230	0.0284
Coef_EC83	RMS (K)	3.8283	0.2040	0.1822	2.8419	0.7107	0.4514	0.8869
Coef_New90	RMS (K)	0.0614	0.0501	0.0402	0.0383	0.0364	0.0380	0.0413
Coefs	Channel	8	9	10	11	12	13	14
Coef_EC83	AVG (K)	-1.0710	-1.6026	-9.5989	-2.2629	-0.3528	-0.0325	-0.6618
Coef_New90	AVG (K)	0.0323	0.0196	0.0062	-0.0019	-0.0038	-0.0035	-0.0022
Coef_EC83	STD (K)	1.1384	6.1034	8.3056	2.3030	0.4600	0.0644	0.8740
Coef_New90	STD (K)	0.1066	0.0978	0.0480	0.0240	0.0182	0.0160	0.0144
Coef_EC83	RMS (K)	1.5630	6.3103	12.6934	3.2287	0.5797	0.0721	1.0963
Coef_New90	RMS (K)	0.1114	0.0998	0.0484	0.0240	0.0186	0.0164	0.0145

combined influence of temperature and water vapor, which ~~decreases~~ reduces the correlation of layer opacity (De Angelis et al., 2016). ~~Fig. 1(b) shows the case under~~ For the 101L UMBC ~~48 dataset. The results show slightly larger biases than those under the 101L ECMWF 83 dataset, as most profiles in the 101L UMBC 48 dataset are not included in the ODPS training process. Specifically, biases at water vapor channels (22.234 GHz - 30 GHz) change most obviously, with RMS values increasing from 0.04 K to 0.06 K at channel 1. This reflects the high sensitivity of BTs at these channels to humidity. Fig. 1(c) and 1(d) show metrics at each channels of HATPRO. The results show similar trends to those for MP3000A. Under the 101L ECMWF 83 dataset, AVGs, STDs, and RMSs are less than 0.019 K, 0.037~~48-profile dataset, results using Coef_New90 demonstrate significantly higher accuracy compared to those using Coef_EC83. In channels 9 and 10, the RMS values for Coef_EC83 exceed 6.0 K, ~~and 0.04~~whereas those for Coef_New90 remain below 0.1 K~~, respectively, for the 7 K-band channels. Biases in channels 8-10 are larger than those in~~ . In other channels, ~~with RMS values of 0.11 K, 0.1 K, and 0.04 K. In contrast, results of ARMS-gb agrees well with MonoRTM for channels 11-14, with a maximum RMS of 0.01 K. Under the 101L UMBC 48 dataset, biases are slightly larger than those under the 101L ECMWF 83 dataset~~the RMS values for Coef_New90 are one to two orders of magnitude smaller than those for Coef_EC83. Since similar results are observed for MP3000A channels, these results are not presented in the paper.

3.2 Effect of Vertical Interpolation

To apply ODPS in RT simulations with profiles having different kinds of vertical coordinates, ~~twice~~ two vertical interpolations are required. Previous studies have investigated the impact of different vertical interpolation modes on RT simulations and Jacobian calculations for the satellite perspective. For instance, Hocking (2014) compared 5 vertical interpolation modes within RTTOV. They found that using various vertical interpolation modes not only affects the simulated BTs, but also impacts Jacobian calculations. This study aims to compare BTs and Jacobians calculated by two different vertical interpolation modes for the GMR perspective. Detailed setups in these modes are summarized as follows:

Mode 1 is the default setting in RTTOV-gb (De Angelis et al., 2016; Cimini et al., 2019). The RTTOV-gb User Guide also strongly recommends not to change the mode. In mode 1, both atmospheric parameters and optical depth are interpolated using the Rochon interpolation (Rochon et al., 2007).

Mode 2 which is employed by ARMS-gb has been previously introduced (see Section 2.2). In mode 2, atmospheric parameters are interpolated using the Rochon interpolation, similar to mode 1. However, for optical depth, the nearest-neighbour log-linear interpolation is used instead. Additionally, before interpolating water vapor, its unit is converted to partial pressure, which allows for more accurate calculations.

~~Comparisons are performed in~~ We implement both interpolation modes within ARMS-gb first and perform comparisons across HATPRO channels. Atmospheric parameters are taken from the 54L ECMWF ~~83 dataset and UMBC 48 dataset. In the benchmark calculation~~83-profile and UMBC 48-profile dataset. For the benchmark calculations, we directly input 54L temperatures and water vapor profiles into MonoRTM without any interpolation. Both mode 1 and mode 2 interpolate profiles into 101L first and then interpolate optical depth back to 54L. To isolate the impact of the interpolation modes and exclude differences related to the training process (e.g., LBL RTMs and the training dataset), only Coef_New90 is used. Fig. 2(a) and

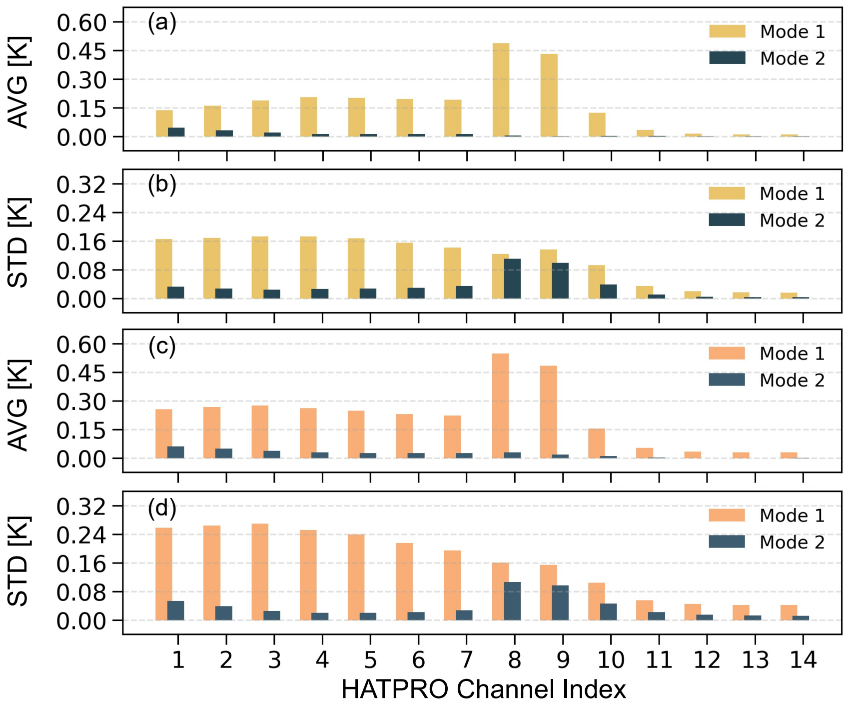

Figure 2. (a) and (b): AVGs and STDs of simulated BTs at 7 observed zenith angles in HATPRO channels. RT simulations for both interpolation mode 1 and 2 performed under the 54L ECMWF ~~83~~ 83-profile dataset. MonoRTM serves as a benchmark to provide reference values for comparison. (c) and (d): Same as (a) and (b), but with RT simulations performed under the 54L UMBC ~~48~~ 48-profile dataset.

2(b) ~~show situations under~~ illustrate results for the 54L ECMWF ~~83~~ 83-profile dataset. In this case, mode 2 ~~is generally more accurate than mode 1.~~ generally outperforms mode 1 in terms of accuracy. In K-band channels, both AVGs and STDs of mode 2 are ~~much less than that~~ significantly lower than those of mode 1. In channel 4, ~~bias drops can reach up to~~ AVG and STD of mode 2 are 0.19 K ~~for AVG~~ and 0.15 K ~~for STD. In channel~~ lower, respectively, compared to mode 1. In channels 8 and 9, AVG ~~of~~ for mode 1 is about 0.45 K while ~~AVG of~~ mode 2 ~~is~~ reduces this bias to less than 0.01 K. STDs ~~of these channels are slightly reduced when we replace mode 1 with mode 2. The slightly reduction of STD is mainly due~~ in these channels also show slight reductions when mode 2 replaces mode 1. This modest reduction in STD is primarily attributed to ODPS regression error ~~whose STD reaches~~ which can reach up to 0.1 K in these ~~two~~ channels. Comparisons are also performed under the 54L UMBC ~~48~~ 48-profile dataset, which ~~contains some profiles with rich water vapor~~ includes profiles with high water vapor content. In channel 3, both AVG and STD ~~of~~ for mode 1 are 0.27 K ~~while AVG and STD of~~ whereas mode 2 ~~are only~~ achieves significantly lower values of 0.04 K and 0.03 K, respectively. In channel 8, AVG ~~of~~ for mode 1 ~~can be~~ reaches as high as 0.55 K while mode 2 reduces ~~these biases to~~ this bias to just 0.03 K. Overall, the results ~~show~~ indicate that mode 2 is generally more accurate than mode 1, ~~especially~~ particularly in channels with strong water vapor absorption.

~~Jacobian calculated by~~ The Jacobians calculated by the two interpolation modes are also different. To evaluate this difference, we use the ~~6-th~~ 6th profile in the 54L UMBC ~~48~~ 48-profile dataset. The profile is selected because it produces significant BT differences between the two modes. The difference reaches up to 0.59 K at observed zenith angle 0° in channel 1. Fig. 3(a), 3(b) and 3(c) show water vapor Jacobian at ~~channel~~ channels 3, 6 and 10, respectively. Jacobian differences between mode 1 and mode 2 are also shown. The results indicate that simulated BTs at channel 3 are very sensitive to water vapor located between 800 hPa and 1000 hPa. The values of water vapor Jacobian in this height range can exceed 5 K/log(g/kg). The maximum value of water vapor Jacobian can reach 7.06 K/log(g/kg) in channel 3 while it is only 1.32 K/log(g/kg) in channel 10. The maximum value of difference between two modes occurs at the first level above ground surface and reaches up to 0.61 K/log(g/kg) in channel 3, 0.55 K/log(g/kg) in channel 6 and 0.14 K/log(g/kg) in channel 10. Situations of temperature Jacobian on channel 11, channel 12 and channel 14 are shown in Fig. 3(d), 3(e) and 3(f), respectively. The simulated BTs at these channels are sensitive to near-surface temperatures below 900 hPa. The maximum values of temperature Jacobian occur at 1033 hPa and can reach up to 0.14 K/K in channel 11, 0.24 K/K in channel 12 and 0.28 K/K in channel 14. Comparing mode 1 with mode 2, we find that, mode 2 reduces temperature Jacobian of channel 14 by 0.007 K/K at 1013 hPa but gives an increase of 0.01 K/K at 1050 hPa. Similar results are also found in channels 11 and 12, but with smaller amplitudes.

Due to its similarity to that for the HATPRO channels, analysis for the MP3000A channels is not presented in the paper.

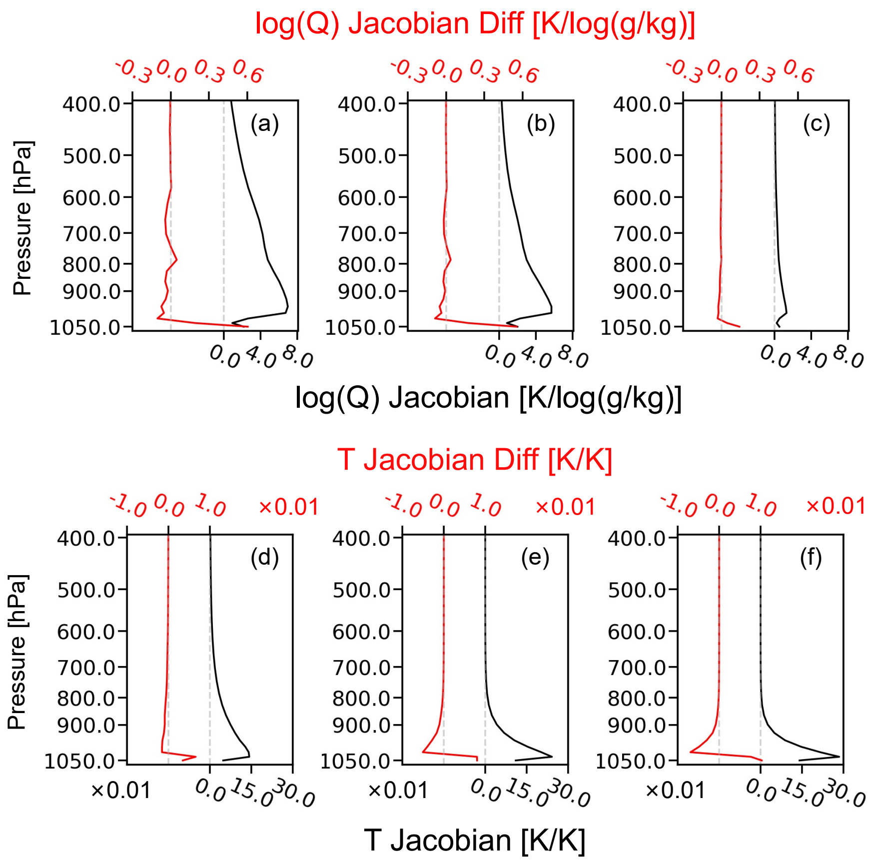

Figure 3. (a), (b) and (c): Water vapor Jacobian analysis for ~~channel~~ channels 3, 6 and 10 of HATPRO. Water vapor Jacobian based on mode 2 is presented as black lines and Jacobian differences between two interpolation modes (mode 2 minus mode 1) are presented as red lines. (d), (e) and (f): Same as (a), (b) and (c) but for temperature Jacobian analysis in different channels. The focus is on channel 11, channel 12, and channel 14 of HATPRO. RT simulations are performed under the ~~6-th~~ 6th profile in the 54L UMBC ~~48~~ 48-profile dataset. Observed zenith angle is set to 0°.

4 Applications in Simulating Real Observations

In this section, we employ ARMS-gb to simulate real observations from GMRs in China. Three GMRs are selected: two are used to provide ~~true reference~~ benchmark values for comparing the accuracy of ARMS-gb and RTTOV-gb, while the third is utilized to demonstrate the ability of ARMS-gb to monitor observational quality. The temperature and water vapor profiles, required as input for RT simulations, are derived from the 137L ERA5 reanalysis dataset. Additionally, direct observations of pressure, temperature, and humidity near the surface, provided by the meteorological sensor onboard GMRs, are also utilized in the RT simulations in this study.

The ERA5 reanalysis dataset (Hersbach et al., 2020) provides an exceptionally detailed representation of the atmosphere, with its 137 vertical levels extending from the surface up to 0.01 hPa. These levels are not uniformly spaced and are more densely packed near the Earth's surface, allowing for a high vertical resolution that accurately captures atmospheric conditions in this height range. This configuration is particularly well-suited for simulating GMRs' observations, as it enables accurate modeling of the PBL. In this study, ERA5 is used with a temporal resolution of 1 hour and a horizontal resolution of $0.25° \times 0.25°$.

Prior to analyzing ~~Observation Minus Background (OMB)~~ OMB based on RT simulations, two essential steps are performed: strict collocation and cloud detection. Collocation involves ensuring that the time and spatial matches between ERA5 reanalysis data and GMR observations are precise. To mitigate biases caused by temporal differences, only observations from GMRs on the hour are selected for analysis. A bilinear interpolation technique is applied to convert atmospheric profiles from the four nearest ERA5 grid points to the specific location of a GMR, using Euclidean-distance-based interpolation weights. Cloud detection involves rejecting observations that meet certain criteria: (1) Observations during rain which are flagged by rain sensors (Cimini et al., 2019); (2) Observations with high sky infrared temperature (>-30°C) (Martinet et al., 2015; De Angelis et al., 2016); (3) Observations with a standard deviation of ~~OMB~~ BTs in the window channel (near 31 GHz) exceeding 0.2 K over a 10-minute period (Turner et al., 2007; Cimini et al., 2019). ~~Finally, RT simulations are performed only under atmospheric profiles where~~ In addition, total column cloud liquid water content and ice water content ~~are both less than~~ from the ERA5 reanalysis dataset are used as another index for cloud clearing. The threshold is set to 100 g/m^2 ~~(Moradi et al., 2020)~~ according to Moradi et al. (2020). We also evaluated OMB statistics under different thresholds (e.g., 10 g/m^2, 1 g/m^2) and results don't noticeably change.

4.1 ~~Compared~~ Comparison to RTTOV-gb

RTTOV-gb is a fast ~~RT model~~ RTM developed at the Center of Excellence in Telesensing of Environment and Model Prediction of Severe Events (CETEMPS). It accounts gaseous absorption by ODPS which is trained by ~~AMSUTRAN (Turner et al., 2019)~~ R98 (Rosenkranz, 1998) or R17 (Rosenkranz, 2017). Additionally, the effects of clouds on observed microwave BTs are also included in RTTOV-gb. A detailed description of the model can be found in De Angelis et al. (2016); Cimini et al. (2019). For a comprehensive comparison between ARMS-gb and RTTOV-gb, please refer to Table ~~3~~4, which summarizes their similarities and differences. In this study, coefficients trained by R98 is used for running RTTOV-gb. It is worth to compare the results of ARMS-gb with those of RTTOV-gb using coefficients trained by R17, a comparison we plan to conduct soon.

The intercomparison period spans from November 1, 2023 to April 30, 2024, covering both winter and spring seasons. Two GMR stations are selected for this study: Karamay, Xinjiang (84.85°E, 45.61°N) and Tanggu, Tianjing (117.79°E, 35.16°N). The altitudes above sea level are 451.6 meters for Karamay and 27 meters for Tanggu. STD of surface pressures from the four nearest ERA5 grid points is approximately 15 hPa for Karamay and 5 hPa for Tanggu, which reflects the situation of surrounding orography. The climate at these two locations is distinct. Karamay has a dry continental climate with low humidity. In contrast, Tanggu experiences a temperate semi-humid monsoon climate with higher humidity. These two stations serve as representative examples of dry and relatively moist environments. The GMRs at both stations provide vertical measurements with an observed zenith angle of 0°. The selection of both time period and station makes it suitable for comparing the performance of ARMS-gb and RTTOV-gb in different atmospheric conditions. Due to the stability of the OMB trend during this period, it is assumed that the quality of the ~~observations is good enough to be used as reference true values for comparison purposes. Due to differences of simulated BTs between two RT models, STD of both ARMS-gb and RTTOV-gb at the window channel are used in the cloud detection process~~calibration may be stable.

The GMR at Karamay is Airda-HTG4. It operates with center frequencies and bandwidths identical to those of HATPRO. Following the collocation and cloud detection steps, a total of 1922 samples remain for analysis. Fig. 4(a-c) present the OMB results obtained from both RTTOV-gb and ARMS-gb. Additionally, we calculate the daily STD using OMB over each individual day. The mean relative differences in daily STD between RTTOV-gb and ARMS-gb are depicted in Fig. 4(d-f). To assess the statistical significance of these differences, a student's T-test is performed, and the corresponding 95 % confidence interval is indicated. This allows for a more rigorous evaluation between the two ~~RT models~~RTMs.

The results ~~of~~ shown in Fig. 4 ~~indicate~~ highlight significant differences in the behavior of ARMS-gb and RTTOV-gb across various channels of Airda-HTG4 at Karamay. In ~~channel~~ channels 1-8, ARMS-gb tends to overestimate BTs. In contrast, the OMB median values of RTTOV-gb are much closer to 0 K in these channels. For instance, in channel 1, the OMB median value of ARMS-gb is -0.98 K, while ~~that of~~ for RTTOV-gb it is only -0.05 K. In ~~channel~~ channels 9 and 10, ~~absolute values of AVGs of~~ the absolute AVG values for ARMS-gb exceed 2 K. RTTOV-gb also ~~overestimate~~ overestimates BTs in these two channels, with AVGs of -1.93 K in channel 9 and -1.34 K in channel 10. Both ARMS-gb and RTTOV-gb demonstrate high accuracy in channels 11-14, ~~with~~ where the OMB median values ~~of both the two models~~ for both RTM are less than 0.3 K. In terms of daily STD, significant differences between the two ~~RT models occur~~ RTMs are observed in four K-band channels (~~channel~~ channels 4-7) and three V-band channels (~~channel~~ channels 11, 13, 14). Specifically, compared to RTTOV-gb, the daily STD of ARMS-gb is reduced by 0.75 % in ~~channel~~ channels 5 and 6. ~~The OMBs of~~ However, RTTOV-gb ~~are more stable than those of~~ shows more stable OMBs than ARMS-gb in three V-band channels~~. The~~, with a mean relative difference of daily STD ~~between the two models is~~ of 1.52 % in channel 14.

Additionally, radiosonde data are also used as input for RT simulations, and the results from RTTOV-gb and ARMS-gb are compared. Scatterplots of simulated versus observed BTs are presented in Fig. 5, focusing on 5 K-band channels and 4 V-band channels. After collocation and cloud detection, 163 samples are evaluated. In the K-band channels, RTTOV-gb simulations

Table 4. The similarities and differences between ARMS-gb and RTTOV-gb.

	ARMS-gb	RTTOV-gb
Training Dataset	101L ECMWF 83-profile dataset plus 7 profiles from 101L UMBC 48-profile dataset	101L ECMWF ~~83~~ 83-profile dataset
LBL Model	MonoRTM	~~AMSUTRAN~~ R98 or R17
Overlap Absorption	Effective Transmittance	
Channel Transmittance	Taking the mean of LBL transmittance within channel bandwidth	
Input Atmospheric Parameters	Temperatures and humidity at each input pressure level	
Input Near Surface Parameters	Temperature, humidity and pressure at 2 m	Temperature and pressure at 2 m
Interpolation Mode	Mode 2 in Section 3.2	Mode 1 in Section 3.2
Predictors	19 for $\Gamma_{\mathrm{ch}}^{\mathrm{mixed}}$; 15 for $\Gamma_{\mathrm{ch}}^{\mathrm{H_2O},*}$	10 for $\Gamma_{\mathrm{ch}}^{\mathrm{mixed}}$; 15 for $\Gamma_{\mathrm{ch}}^{\mathrm{H_2O},*}$
Vertical Distribution of Planck Function	Linear in tau approximation	

align more closely with observations compared to ARMS-gb, exhibiting smaller OMB median values and STDs. ARMS-gb tends to overestimate observations, consistent with the results in Fig. 4. In the V-band channels, RT simulation accuracy is generally higher than in the K-band channels, with correlation coefficients approaching 1.0. The OMB median values and STDs from ARMS-gb are slightly lower than those from RTTOV-gb.

The GMR at Tanggu, YKW3, shares the same center frequencies and bandwidths as MP3000A. Fig. ~~5~~6(a-c) present the OMB results of the two ~~RT models~~ RTMs based on 1845 statistical data. Notably, BTs simulated by ARMS-gb are more closely aligned with observations than those of RTTOV-gb in ~~channel~~ channels 1-8. In particular, the OMB median values of RTTOV-gb show significant deviations from 0 K, with values reaching 3.28 K in channel 1 and 0.69 K in channel 8. In contrast, ARMS-gb exhibits more accurate results, with OMB median values of ~~only~~ 2.44 K in channel 1 and 0.26 K in channel ~~1 and 8, respectively. In channel~~ 8. In channels 12, 13, and 14, the AVG of RTTOV-gb are more closely aligned with 0 K than those of ARMS-gb. Both ARMS-gb and RTTOV-gb ~~display~~ demonstrate similar accuracy in ~~channel~~ channels 16-22, with differences in OMB median values between the two ~~models~~ RTM being less than 0.1 K. Fig. ~~5~~6(d-f) show the mean relative differences in daily STD between ARMS-gb and RTTOV-gb. In channel 2, the daily STD of RTTOV-gb is 0.98 % ~~less~~ lower than that of ARMS-gb. Conversely, in ~~channel~~ channels 9-16, the daily STD of ARMS-gb is significantly ~~less~~ lower than that of RTTOV-gb, with ~~a maximum relative difference occurring~~ the largest relative difference occurs in channel 12 ~~and reaching~~ at 2.59 %.

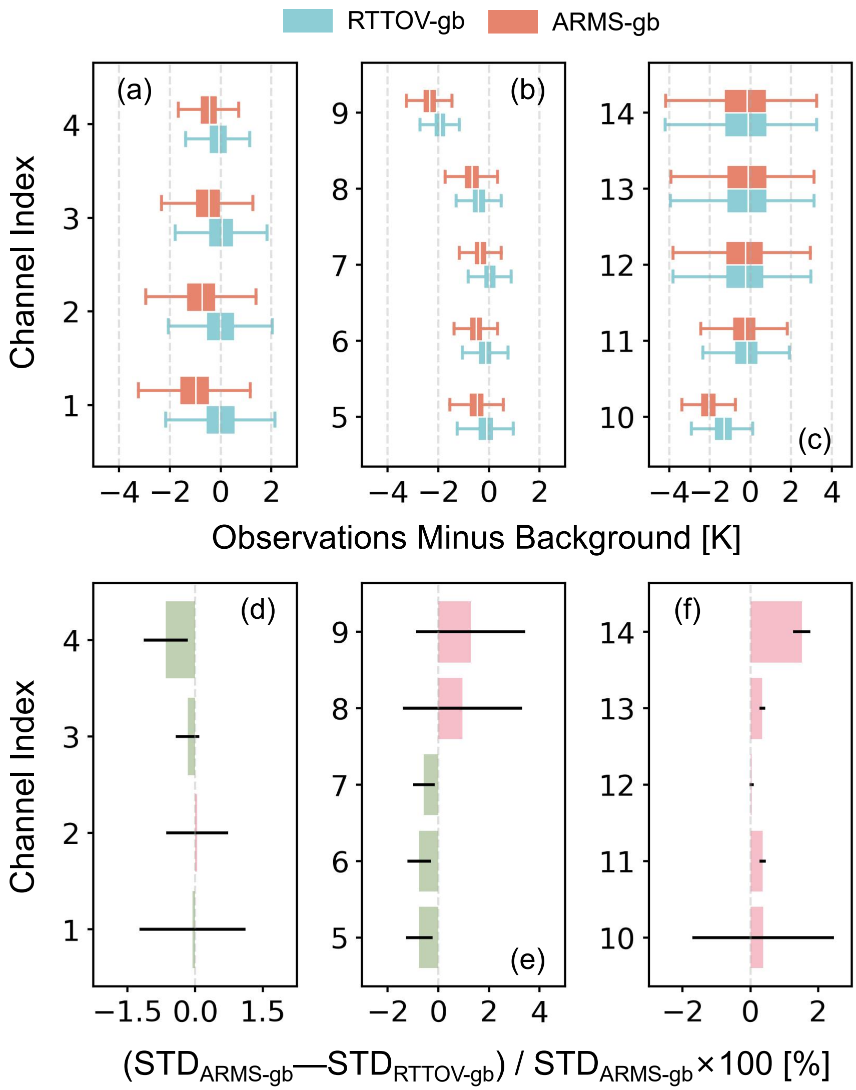

Figure 4. (a-c): OMB of RTTOV-gb and ARMS-gb during the period from November 1, 2023 to April 30, 2024. Observations are from Airda-HTG4 at Karamay. RT simulations are performed under the 137L ERA5 reanalysis dataset. White markers indicate the median values of each distribution. (d-f) Mean relative differences in daily STD between RTTOV-gb and ARMS-gb. Daily STD values are calculated using OMB within each single day. Black bars represent the 95 % confidence range, indicating the statistical significance of these differences.

The ~~minimum value of~~ smallest relative difference occurs in channel 16, at 0.22 %. OMB ~~of~~ results from ARMS-gb ~~are also slightly more stable than that~~ also show slightly greater stability than those of RTTOV-gb in ~~channel~~ channels 17-22.

Similar to the Karamay case, RT simulations for the Tanggu case are also conducted using radiosonde data. Simulated BTs from both ARMS-gb and RTTOV-gb are compared with observations, as shown in Fig. 7. After collocation and cloud detection,

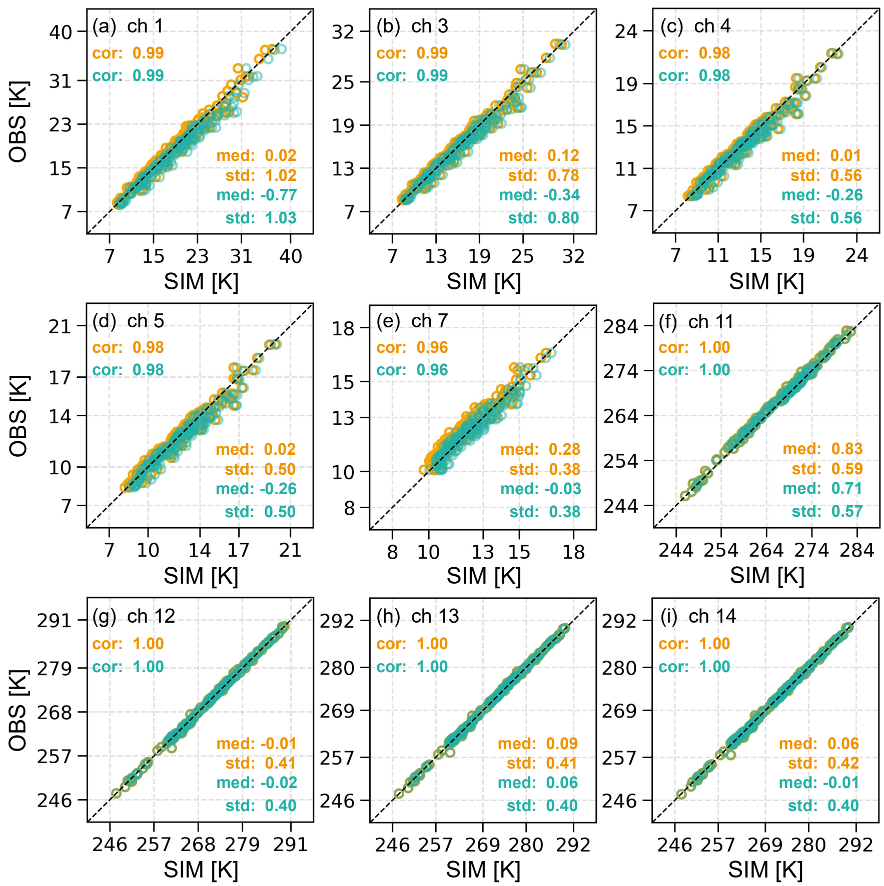

Figure 5. Scatter of simulated vs. observed BTs for 9 out of the 14 channels of Airda-HTG4 at Karamay from November 1, 2023 to April 30, 2024. RT simulations are performed using radiosonde data. Orange represents results of RTTOV-gb; Green represents results of ARMS-gb. After collocation and cloud detection, a total of 163 samples are analyzed in this case. The panel reports the correlation coefficients (cor), as well as the median values (med) and standard deviations (std) of OMB.

148 samples are included in the comparison, with 12 out of the 22 channels selected for analysis. In channels 1 and 2, both RTTOV-gb and ARMS-gb underestimate BTs. However, ARMS-gb provides more accurate results than RTTOV-gb, with higher correlation coefficients and smaller OMB median values and STDs. In channels 4, 6, 7 and 8, the OMB median values from ARMS-gb are closer to 0 K, while RTTOV-gb shows smaller STDs of OMB. For channels with central frequencies ranging from 54.5 GHz to 58.8 GHz, both RTTOV-gb and ARMS-gb accurately simulate observed BTs, with correlation coefficients for both RTMs reaching up to 0.98. The OMB median values and STD from ARMS-gb are slightly lower than those from RTTOV-gb.

Performance of fast ~~RT models~~ RTMs is influenced by several factors. A detailed description of channel characteristics and the accuracy of the LBL model used for training are crucial in achieving accurate RT simulations. Moreover, the quality of

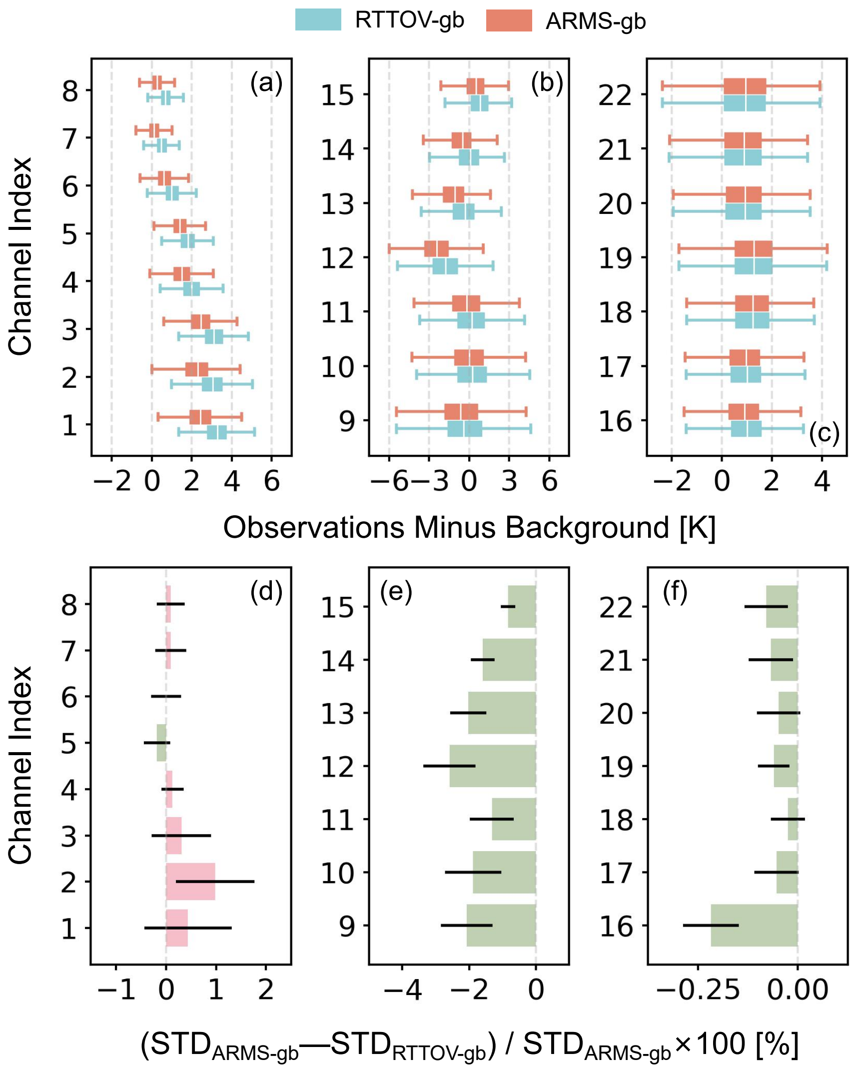

Figure 6. Same as Fig. 4, but show.the situation of YKW3 at Tanggu.

the input profiles themselves can be a significant limitation. For instance, temperatures from ERA5 reanalysis data have been shown to have large systematic errors at altitudes between 2000-3000 m and relative humidity errors ranging from 40 % to 100 % over the range of 500-2500 m (Wei et al., 2024). This highlights the challenge in relying on current reanalysis data for accurate thermal variables, particularly in the PBL. Furthermore, channel characteristics play a significant role in RT simulations, especially when considering the SRF information. Studies have demonstrated that incorporating SRF information can lead to substantial improvements in RT simulations from a satellite perspective (Moradi et al., 2020; Chen et al., 2021;

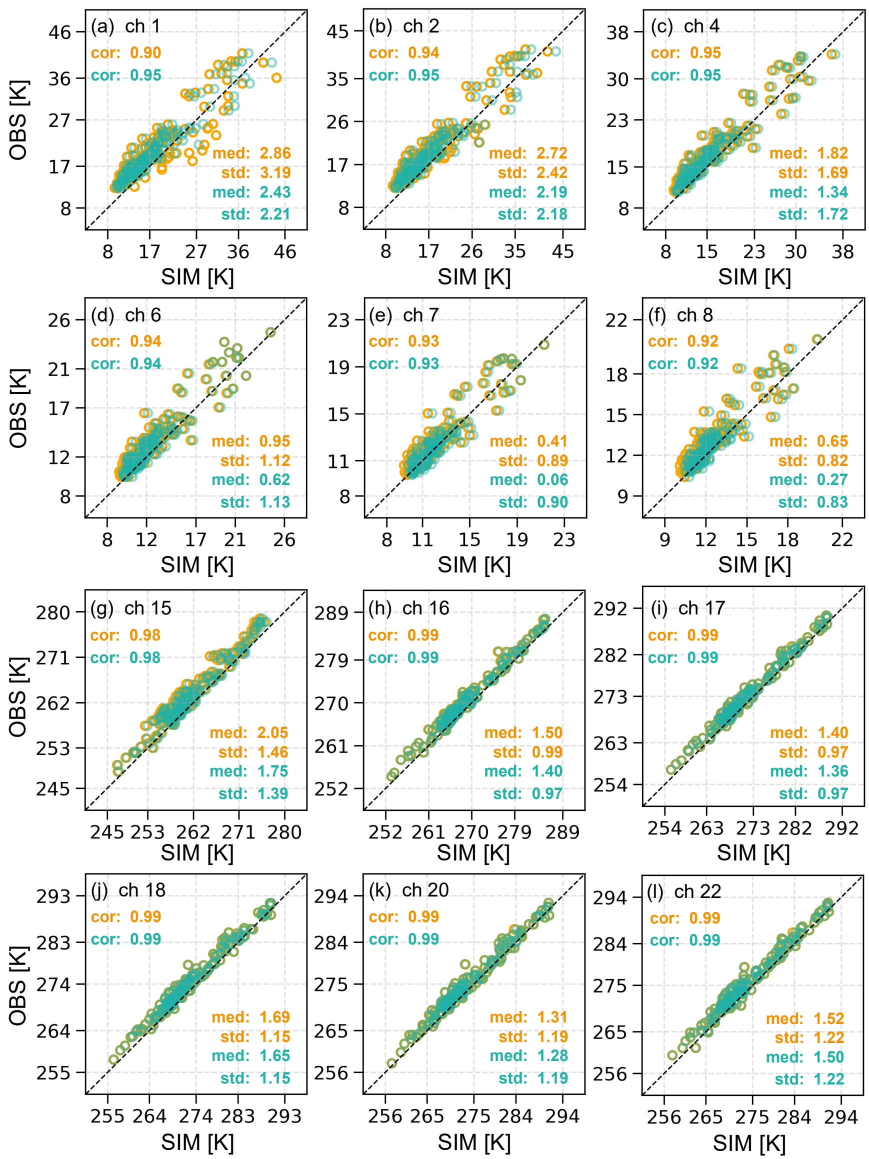

Figure 7. Same as Fig. 5, but shows results for 12 out of the 22 channels of YKW3 at Tanggu from November 1, 2023 to April 30, 2024. After collocation and cloud detection, a total of 148 samples are analyzed in this case.

Kan et al., 2024). We believe that incorporating SRF information could also enhance the accuracy of both RTTOV-gb and ARMS-gb.

4.2 Monitoring Observational Qualities

ARMS-gb offers real-time OMB information, which provides valuable guidance for evaluating observational qualities. This is particularly important in assimilating GMR data in NWP. In this study, ARMS-gb is applied to monitor the quality of observations from Airda-HTG4 located at Minfeng, Xinjiang (82.69°E, 37.07°N). The station's altitude above sea level is 1410 meters, and STD of surface pressures from the four nearest ERA5 grid points is about 6 hPa. The time period examined ~~is~~ spans from September 1, 2023, to November 30, 2023. After collocation and cloud detection, 1922 samples are retained for analysis.

The observational BTs as well as OMB of ARMS-gb in ~~channel~~ channels 1, 8 and 14 are presented in Fig. ~~6. Channel~~ 8. Channels 1 and 14 serve as representatives of water vapor and temperature channels, respectively, while channel 8 is influenced by both water vapor and temperature. Insights from the OMB results for channel 1 indicate that STD can be significantly reduced through calibration, decreasing from 2.03 K to 0.98 K. The calibration time can also be clearly identified in the OMB series of channel 8. Both AVG and STD values change noticeably before and after the calibration time. Specifically, AVG and STD reach 4.60 K and 0.61 K in September, respectively, but are reduced to -0.52 K and 0.33 K after calibration. In contrast, observational BTs of channel 14 show little sensitivity to calibration. Both AVG and STD values for this channel remain largely unchanged, with only some negative OMB values occurring during a short time period around the calibration time. The observation series of these three channels highlights that it is challenging to evaluate the quality of observations without access to OMB information. The results from ARMS-gb provide valuable insights into observational qualities.

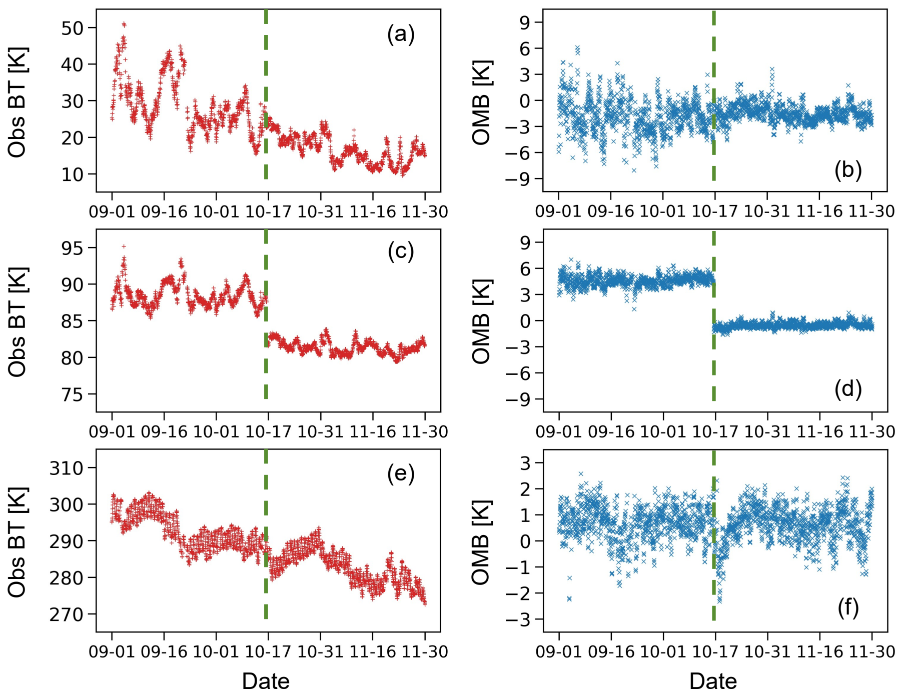

Figure 8. (a) and (b): Observations for channel 1 from Airda-HTG4 at Minfeng during September 1, 2023 to November 30, 2023 along with the corresponding OMB series of ARMS-gb. (c) and (d): Same as (a) and (b) but show situations of channel 8. (e) and (f): Same as (a) and (b) but show situations of channel 14. The green dashed line indicates the calibration time.

5 Summary and Conclusions

GMRs can provide continuous observations with high temporal resolution. These observations are particularly useful for monitoring rapid changes of temperature and humidity within the PBL. As a result, direct assimilation of GMR observations has great potential in improving the performance of NWP, especially for the lowest few kilometres of the atmosphere. In this study, we propose a RTM, ARMS-gb, capable of simulating BTs observed by GMRs. ARMS-gb can be used as an observation operator to map atmospheric parameters into observations in a data assimilation system.

ARMS-gb is developed based on a clear-sky RT solver that accounts for atmospheric thermal emissions from TOA to the ground surface, as well as the effects of gaseous absorption. An accurate description of gaseous absorption is critical for the performance of RT simulations. To address this issue, ~~we employ~~ ARMS-gb employs ODPS, which utilizes the 101L ECMWF ~~83 profiles~~ 83-profile dataset as its primary training dataset. This dataset is augmented with seven additional profiles from ~~UMBC 48 to improve simulation accuracy~~ the 101L UMBC 48-profile dataset. The humidity range of these additional profiles exceeds the mean values plus the standard deviation of the ECMWF 83-profile dataset, particularly in the low levels of the troposphere. This augmentation enhances the simulation accuracy of ARMS-gb, particularly in moist environments. In ODPS, MonoRTM is employed to calculate the LBL transmittance at 7 observed zenith angles. To apply ODPS in RT simulations with profiles having different types of vertical coordinates, ~~twice~~ two vertical interpolations are required. In ARMS-gb, temperatures and water vapors from input pressure levels are remapped onto the ~~101 levels~~ 101L using the Rochon interpolation for calculating predictors. The resulting optical depth values are interpolated back to the original input pressure levels via a nearest-neighbour log-linear interpolation. Additionally, before interpolating water vapor, its unit is converted to partial pressure, which allows for more accurate calculations. To satisfy the requirements of its applications in remote sensing and data assimilation, we also develop the tangent linear as well as adjoint module of ARMS-gb and derive the analytical ~~Jacobian~~ K matrix.

ARMS-gb currently supports two types of GMRs: ~~the HATPRO and the~~ HATPRO and MP3000A. ~~The accuracy of ARMS-gb is evaluated by comparing its results to those obtained from MonoRTM~~To evaluate the impact of enriching the training dataset, two sets of fitting coefficients are trained: one using the ECMWF 83-profile dataset (Coef_EC83) and the other using the new training dataset (Coef_New90). Profiles from the ~~ECMWF 83 dataset and the UMBC 48~~ 101L ECMWF 83-profile and UMBC 48-profile dataset are used as input for RT simulations. ~~In~~ MonoRTM serves as the benchmark to provide reference values for comparison. For the 101L ~~case, ARMS-gb shows high accuracy with RMS values less than 0.12~~ECMWF 83-profile dataset, the accuracy of the two fitting coefficients is comparable, with the maximum RMS difference between them being only 0.0078 K~~for all observed channels of MP3000A. Biases for channels between 51 GHz and 54 GHz are larger than those for other channels, with a maximum RMS of 0.11 K at channel 9. The results in HATPRO channels show similar trends to those for MP3000A. Simulated BTs and Jacobian calculated by two different~~. However, for the 101L UMBC 48-profile dataset, Coef_New90 demonstrates significantly higher accuracy compared to Coef_EC83. The RMS values of Coef_New90 are one to two orders of magnitude smaller than those of Coef_EC83. Additionally, the effects of vertical interpolation modes ~~are compared to each other~~ on forward and Jacobian calculations are evaluated from the perspective of ~~HATRPO channels.~~ HATPRO channels. Two different vertical interpolation modes are considered: Mode 1~~is~~, the default setting in RTTOV-gb~~while~~, and mode 2~~is~~

, employed by ARMS-gb. To isolate the impact of the interpolation modes, only Coef_New90 is used to exclude differences related to the training process. Under the 54L ECMWF ~~83~~ 83-profile dataset, mode 2 ~~is generally more accurate than~~ generally outperforms mode 1, ~~especially~~ particularly in channels with strong water vapor absorption. ~~In~~ For example, in channel 4, ~~bias drops can reach up to~~ AVG and STD using mode 2 are 0.19 K ~~for AVG~~ and 0.15 K ~~for STD. In channel~~ lower, respectively, compared to mode 1. In channels 8 and 9, AVG ~~of~~ for mode 1 is ~~about~~ approximately 0.45 K~~while AVG of~~, while for mode 2, it is less than 0.01 K. STDs ~~of these channels are slightly reduced when we replace~~ in these channels also show slight reductions when mode 1 is replaced with mode 2. ~~Jacobian calculated by~~ The Jacobian values calculated by the two interpolation modes are also different. Comparing mode 1 with mode 2, ~~we find~~ it is observed that mode 2 reduces the temperature Jacobian of channel 14 by 0.007 K/K at 1013~~hPa but gives an increase of~~ hPa but increases it by 0.01 K/K at 1050 hPa. In terms of the water vapor Jacobian, the maximum ~~value of difference between~~ difference between the two modes occurs at the first level above the ground surface. ~~The difference can reach~~ In channel 3, this difference reaches up to 0.61 K/log(g/kg)~~in channel 3 while~~, while in channel 10, it is only 0.14 K/log(g/kg)~~in channel 10.~~.

To further validate the performance of ARMS-gb, we apply it in simulating real observations from GMRs and ~~compares~~ compare its results to ~~that~~ those of RTTOV-gb. Input atmospheric parameters, such as temperature and water vapor profiles, are derived from the 137L ERA5 reanalysis dataset. The intercomparison period spans from November 1, 2023 to April 30, ~~2024 and we select observations from~~ 2024. Airda-HTG4 located at Karamay, Xinjiang (84.85°E, 45.61°N) and YKW3 located at Tanggu, Tianjing (117.79°E, 35.16°N) ~~as true reference values~~provide actual observations. Significant differences are ~~shown~~ observed in the behavior of ARMS-gb and RTTOV-gb across various channels of Airda-HTG4 at Karamay. In ~~channel~~ channels 1-8, ARMS-gb tends to overestimate BTs, whereas the OMB median values of RTTOV-gb are much closer to 0 K in these channels. Both ~~two RTM~~ RTMs demonstrate high accuracy in channels 11-14. In terms of daily STD, ~~compared to~~ ARMS-gb outperform RTTOV-gb ~~,~~ in channels 5 and 6, reducing the daily STD ~~of ARMS-gb is reduced~~ by 0.75 %~~in channel 5 and 6 but is~~. However, in channel 14, the daily STD for ARMS-gb increased by 1.52 % ~~in channel 14. In the case of Tanggu~~compared to RTTOV-gb. Furthermore, radiosonde data are also used as input for RT simulations, and the results from RTTOV-gb and ARMS-gb are compared. In the K-band channels, ARMS-gb tends to overestimate observations, consistent with the results derived from the 137L ERA5 reanalysis dataset. RTTOV-gb simulations exhibit smaller OMB median values and STDs. In the V-band channels, simulations of both RTTOV-gb and ARMS-gb show high accuracy, with correlation coefficients approaching 1.0.

Under the 137L ERA5 reanalysis dataset, BTs simulated by ARMS-gb are more closely aligned with observations from YKW3 at Tanggu than those of RTTOV-gb in ~~channel~~ channels 1-8. The daily STD of ARMS-gb is ~~less~~ lower than that of RTTOV-gb in ~~channel~~ channels 9-22~~with a~~, with the maximum relative difference ~~occurring~~ observed in channel 12~~and~~, reaching 2.59 %. ~~We also~~ Similar to the Karamay case, RT simulations are also conducted using radiosonde data for the Tanggu case. The results show that the OMB median values from ARMS-gb are closer to 0 K in most YKW3 channels. Notably, in channels 1 and 2, ARMS-gb provides more accurate results than RTTOV-gb, with higher correlation coefficients and smaller OMB median values and STDs. For channels with central frequencies ranging from 54.5 GHz to 58.8 GHz, both RTTOV-gb and ARMS-gb accurately simulate observed BTs, with correlation coefficients for both RTMs reaching up to 0.98.

To demonstrate the ability of ARMS-gb to monitor observational quality, we utilize observations from Airda-HTG4 located at Minfeng, Xinjiang (82.69°E, 37.07°N)~~to demonstrate the ability of ARMS-gb to monitor observational quality~~. The calibration time can be clearly identified in the OMB series of channel 1 and 8. In contrast, observational BTs of channel 14 show little sensitivity to calibration. Compared to observation series, OMB information from ARMS-gb provides more valuable insights into observational qualities of GMRs.

We believe that the performance of ARMS-gb can be further ~~improved~~ enhanced by incorporating SRF information into ODPS. Selecting a reliable and accurate LBL model for training is also ~~considered essential for enhancing~~ essential for improving the accuracy of RT simulations. For example, Larosa et al. (2024) incorporates the latest advancements in absorption spectroscopy to improve RT simulation accuracy in the 50-54 GHz frequency range. An intercomparison among different microwave LBL RTMs is necessary to construct a reliable transmittance dataset for the ODPS training process. In addition, we plan to integrate a particle scattering module into ARMS-gb in the near future~~to~~, which will extend its capabilities ~~and~~ to enable simulations under all-sky conditions. With the development of ARMS-gb, research ~~about~~ on the direct assimilation of ~~GMRs' observations~~ GMR observations into NWP will be carried out soon.

Code and data availability. RTTOV-gb can be downloaded from the EUMETSAT NWP SAF website https://nwp-saf.eumetsat.int/site/software/rttov-gb/ and MonoRTM is available at https://github.com/AER-RC/monoRTM/. The 137-level ERA5 reanalysis data is available from Copernicus Climate Data Store https://climate.copernicus.eu/climate-reanalysis. Observations from GMRs at Karamay, Tanggu and Minfeng used in this study can be obtained from China Meteorological Administration Data As A Service (CMADaaS) under an available license. Codes of ARMS-gb are available at https://zenodo.org/records/14032776.

Appendix A: Predictors for Optical Depth Regression

In this section, predictors for optical depth regression are specified. These predictors also refer to Matricardi et al. (2004); De Angelis et al. (2016). ~~Variables used in the predictors calculation.~~ $\cancel{P_{\delta P}(j) = P(j+1)[P(j+1) - P(j)]}$ $\cancel{T(j) = (T^{\mathrm{prof}}(j) + T^{\mathrm{prof}}(j+1))/2}$ $\cancel{T^*(j) = (T^{\mathrm{ref}}(j) + T^{\mathrm{ref}}(j+1))/2}$ $\cancel{Q(j) = (Q^{\mathrm{prof}}(j) + Q^{\mathrm{prof}}(j+1))/2}$ $\cancel{Q^*(j) = (Q^{\mathrm{ref}}(j) + Q^{\mathrm{ref}}(j+1))/2}$ $\cancel{T_r(j) = T(j)/T^*(j)}$ $\cancel{T_w(j) = P_{\delta P}(j) T_r(j)}$ $\cancel{dT(j) = T(j) - T^*(j)}$ $\cancel{dT_2(j) = dT(j)|dT(j)|}$ $\cancel{Q_r(j) = Q(j)/Q^*(j)}$

In Table A1, θ is the local zenith angle. In the optical depth calculation, θ varys with height and then the Earth curvature effect is taken into account (Chen et al., 2012).

As mentioned in section 2, the predictors calculation is performed on the fixed 101 levels. Correspondingly, in Table ~~A1~~A2, j varys from 1 to 100 and refers to the j-th atmospheric layer. T^{prof} (unit: K) and Q^{prof} (unit: g/kg) are input temperature and water vapor mass mixing ratio. Both of them have been interpolated into the fixed 101 levels before the predictors calculation. T^{ref} and Q^{ref} are same as T^{prof} and Q^{prof} but from the reference profile. The reference profile is usually obtained by taking the mean over the training dataset. We note that, $T_w(100)$ is set to 0 (De Angelis et al., 2016).

~~In Table A2, θ is the local zenith angle. In the optical depth calculation, θ varys with height and then the Earth curvature effect is taken into account (Chen et al., 2012).~~

Table A1. The predictors pool used for optical depth regression.

Predictor	Mixed Gas	Water Vapor
1	$\sec(\theta)$	$[\sec(\theta)Q_r]^2$
2	$\sec(\theta)T_r$	$[\sec(\theta)Q_{\mathrm{zp}}]^2$
3	$\sec(\theta)[T_r]^2$	$[\sec(\theta)Q_{\mathrm{zp}}]^4$
4	T_r	$\sec(\theta)Q_r dT$
5	$\sec^2(\theta)$	$\sqrt{\sec(\theta)Q_r}$
6	$[T_r]^2$	$[\sec(\theta)Q_r]^{0.25}$
7	$\sec(\theta)T_{\mathrm{zp}}$	$\sec(\theta)Q_r$
8	$\sec(\theta)[T_r]^3$	$[\sec(\theta)Q_r]^3$
9	$\sec(\theta)\sqrt{\sec(\theta)T_r}$	$[\sec(\theta)Q_r]^4$
10	$\sec(\theta)T_w$	$\sec(\theta)Q_r dT_2$
11	$\sec(\theta)T_w/T_r$	$\sqrt{\sec(\theta)Q_r}dT$
12	$\sqrt{\sec(\theta)}$	$[\sec(\theta)Q_r]^2/Q_{\mathrm{zp}}$
13	$\sqrt{\sec(\theta)}[T_w]^{0.25}$	$\sqrt{\sec(\theta)Q_r}Q_r/Q_{\mathrm{zp}}$
14	$\sec(\theta)dT/[T_r]^2$	$\sec(\theta)[Q_r]^2/T_r$
15	$\sec(\theta)dT_2/[T_r]^2$	$\sec(\theta)[Q_r]^2/[T_r]^4$
16	$\sec(\theta)dT/T_r$	
17	$\sec(\theta)dT_2/T_r$	
18	$\sec(\theta)dT$	
19	$\sec(\theta)dT_2$	

Table A2. Variables used in the predictors calculation.

$P_{\delta P}(j) = P(j+1)[P(j+1) - P(j)]$	
$T(j) = (T^{\mathrm{prof}}(j) + T^{\mathrm{prof}}(j+1))/2$	$T^*(j) = (T^{\mathrm{ref}}(j) + T^{\mathrm{ref}}(j+1))/2$
$Q(j) = (Q^{\mathrm{prof}}(j) + Q^{\mathrm{prof}}(j+1))/2$	$Q^*(j) = (Q^{\mathrm{ref}}(j) + Q^{\mathrm{ref}}(j+1))/2$
$T_r(j) = T(j)/T^*(j)$	$T_w(j) = P_{\delta P}(j)T_r(j)$
$T_{\mathrm{zp}}(j) = \sum_{k=N}^{j} P_{\delta P}(k)T(k) / \sum_{k=1}^{j} P_{\delta P}(k)T^*(k)$	
$dT(j) = T(j) - T^*(j)$	$dT_2(j) = dT(j)\lvert dT(j)\rvert$
$Q_r(j) = Q(j)/Q^*(j)$	
$Q_{\mathrm{zp}}(j) = \sum_{k=N}^{j} P_{\delta P}(k)Q(k) / \sum_{k=N}^{j} P_{\delta P}(k)Q^*(k)$	

Author contributions. YS developed the model code and prepared the initial draft. JY and WH offered the conception of the study and led the model development. LH and JM dealt with the data used in validations. All authors discussed this work and reviewed the manuscript.

Competing interests. The authors declare that they have no conflict of interest

Acknowledgements. This research was funded by the National Key Research and Development Program of China (2021YFB3900400); the National Natural Science Foundation of China (U2142212, 42305162); Hunan Provincial Natural Science Foundation of China (2021JC0009). We appreciate the topic editor and two anonymous reviewers for their valuable comments.

References

Cady-Pereira, K. E., Turner, E. C., and Saunders, R. W.: Inter-comparison of line-by-line radiative transfer models MonoRTM and AMSU-TRAN for microwave frequencies from the Top-Of-Atmosphere, https://nwp-saf.eumetsat.int/publications/vs_reports/nwpsaf-mo-vs-057.pdf, 2021.

Cao, Y., Shi, B., Zhao, X., Yang, T., and Min, J.: Direct Assimilation of Ground-Based Microwave Radiometer Clear-Sky Radiance Data and Its Impact on the Forecast of Heavy Rainfall, Remote Sensing, 15, https://doi.org/10.3390/rs15174314, 2023.

Caumont, O., Cimini, D., Löhnert, U., Alados-Arboledas, L., Bleisch, R., Buffa, F., Ferrario, M. E., Haefele, A., Huet, T., Madonna, F., and Pace, G.: Assimilation of humidity and temperature observations retrieved from ground-based microwave radiometers into a convective-scale NWP model, Quarterly Journal of the Royal Meteorological Society, 142, 2692–2704, https://doi.org/https://doi.org/10.1002/qj.2860, 2016.

Chen, H., Han, W., Wang, H., Pan, C., An, D., Gu, S., and Zhang, P.: Why and How Does the Actual Spectral Response Matter for Microwave Radiance Assimilation?, Geophysical Research Letters, 48, e2020GL092 306, https://doi.org/https://doi.org/10.1029/2020GL092306, 2021.

Chen, Y., Han, Y., Van Delst, P., and Weng, F.: On water vapor Jacobian in fast radiative transfer model, Journal of Geophysical Research: Atmospheres, 115, https://doi.org/https://doi.org/10.1029/2009JD013379, 2010.

Chen, Y., Han, Y., and Weng, F.: Comparison of two transmittance algorithms in the community radiative transfer model: Application to AVHRR, Journal of Geophysical Research: Atmospheres, 117, https://doi.org/https://doi.org/10.1029/2011JD016656, 2012.

Cimini, D., Hewison, T., Martin, L., Güldner, J., Gaffard, C., and Marzano, F.: Temperature and humidity profile retrievals from ground-based microwave radiometers during TUC, Meteorologische Zeitschrift, 15, 45–56, https://doi.org/10.1127/0941-2948/2006/0099, 2006.

Cimini, D., Rosenkranz, P. W., Tretyakov, M. Y., Koshelev, M. A., and Romano, F.: Uncertainty of atmospheric microwave absorption model: impact on ground-based radiometer simulations and retrievals, Atmospheric Chemistry and Physics, 18, 15 231–15 259, https://doi.org/10.5194/acp-18-15231-2018, 2018.

Cimini, D., Hocking, J., De Angelis, F., Cersosimo, A., Di Paola, F., Gallucci, D., Gentile, S., Geraldi, E., Larosa, S., Nilo, S., Romano, F., Ricciardelli, E., Ripepi, E., Viggiano, M., Luini, L., Riva, C., Marzano, F. S., Martinet, P., Song, Y. Y., Ahn, M. H., and Rosenkranz, P. W.: RTTOV-gb v1.0 – updates on sensors, absorption models, uncertainty, and availability, Geoscientific Model Development, 12, 1833–1845, https://doi.org/10.5194/gmd-12-1833-2019, 2019.

Clough, S., Shephard, M., Mlawer, E., Delamere, J., Iacono, M., Cady-Pereira, K., Boukabara, S., and Brown, P.: Atmospheric radiative transfer modeling: a summary of the AER codes, Journal of Quantitative Spectroscopy and Radiative Transfer, 91, 233 – 244, https://doi.org/https://doi.org/10.1016/j.jqsrt.2004.05.058, 2005.

De Angelis, F., Cimini, D., Hocking, J., Martinet, P., and Kneifel, S.: RTTOV-gb – adapting the fast radiative transfer model RTTOV for the assimilation of ground-based microwave radiometer observations, Geoscientific Model Development, 9, 2721–2739, https://doi.org/10.5194/gmd-9-2721-2016, 2016.

De Angelis, F., Cimini, D., Löhnert, U., Caumont, O., Haefele, A., Pospichal, B., Martinet, P., Navas-Guzmán, F., Klein-Baltink, H., Dupont, J.-C., and Hocking, J.: Long-term observations minus background monitoring of ground-based brightness temperatures from a microwave radiometer network, Atmospheric Measurement Techniques, 10, 3947–3961, https://doi.org/10.5194/amt-10-3947-2017, 2017.

Errico, R. M.: What Is an Adjoint Model?, Bulletin of the American Meteorological Society, 78, 2577 – 2592, https://doi.org/10.1175/1520-0477(1997)078<2577:WIAAM>2.0.CO;2, 1997.

Gordon, I., Rothman, L., Hargreaves, R., Hashemi, R., Karlovets, E., Skinner, F., Conway, E., Hill, C., Kochanov, R., Tan, Y., Wcisło, P., Finenko, A., Nelson, K., Bernath, P., Birk, M., Boudon, V., Campargue, A., Chance, K., Coustenis, A., Drouin, B., Flaud, J., Gamache, R., Hodges, J., Jacquemart, D., Mlawer, E., Nikitin, A., Perevalov, V., Rotger, M., Tennyson, J., Toon, G., Tran, H., Tyuterev, V., Adkins, E., Baker, A., Barbe, A., Canè, E., Császár, A., Dudaryonok, A., Egorov, O., Fleisher, A., Fleurbaey, H., Foltynowicz, A., Furtenbacher, T., Harrison, J., Hartmann, J., Horneman, V., Huang, X., Karman, T., Karns, J., Kassi, S., Kleiner, I., Kofman, V., Kwabia–Tchana, F., Lavrentieva, N., Lee, T., Long, D., Lukashevskaya, A., Lyulin, O., Makhnev, V., Matt, W., Massie, S., Melosso, M., Mikhailenko, S., Mondelain, D., Müller, H., Naumenko, O., Perrin, A., Polyansky, O., Raddaoui, E., Raston, P., Reed, Z., Rey, M., Richard, C., Tóbiás, R., Sadiek, I., Schwenke, D., Starikova, E., Sung, K., Tamassia, F., Tashkun, S., Vander Auwera, J., Vasilenko, I., Vigasin, A., Villanueva, G., Vispoel, B., Wagner, G., Yachmenev, A., and Yurchenko, S.: The HITRAN2020 molecular spectroscopic database, Journal of Quantitative Spectroscopy and Radiative Transfer, 277, 107 949, https://doi.org/https://doi.org/10.1016/j.jqsrt.2021.107949, 2022.

Hersbach, H., Bell, B., Berrisford, P., Hirahara, S., Horányi, A., Muñoz-Sabater, J., Nicolas, J., Peubey, C., Radu, R., Schepers, D., Simmons, A., Soci, C., Abdalla, S., Abellan, X., Balsamo, G., Bechtold, P., Biavati, G., Bidlot, J., Bonavita, M., De Chiara, G., Dahlgren, P., Dee, D., Diamantakis, M., Dragani, R., Flemming, J., Forbes, R., Fuentes, M., Geer, A., Haimberger, L., Healy, S., Hogan, R. J., Hólm, E., Janisková, M., Keeley, S., Laloyaux, P., Lopez, P., Lupu, C., Radnoti, G., de Rosnay, P., Rozum, I., Vamborg, F., Villaume, S., and Thépaut, J.-N.: The ERA5 global reanalysis, Quarterly Journal of the Royal Meteorological Society, 146, 1999–2049, https://doi.org/https://doi.org/10.1002/qj.3803, 2020.

Hocking, J.: Interpolation methods in the RTTOV radiative transfer model, https://digital.nmla.metoffice.gov.uk/download/file/digitalFile_911bd873-f30f-4617-9810-ad73b5457ea1, 2014.

Hocking, J., Vidot, J., Brunel, P., Roquet, P., Silveira, B., Turner, E., and Lupu, C.: A new gas absorption optical depth parameterisation for RTTOV version 13, Geoscientific Model Development, 14, 2899–2915, https://doi.org/10.5194/gmd-14-2899-2021, 2021.

Illingworth, A. J., Cimini, D., Haefele, A., Haeffelin, M., Hervo, M., Kotthaus, S., Löhnert, U., Martinet, P., Mattis, I., O'Connor, E. J., and Potthast, R.: How Can Existing Ground-Based Profiling Instruments Improve European Weather Forecasts?, Bulletin of the American Meteorological Society, 100, 605 – 619, https://doi.org/10.1175/BAMS-D-17-0231.1, 2019.

Kan, W., Shi, Y.-N., Yang, J., Han, Y., Hu, H., and Weng, F.: Improvements of the Microwave Gaseous Absorption Scheme Based on Statistical Regression and Its Application to ARMS, Journal of Geophysical Research: Atmospheres, 129, e2024JD040 732, https://doi.org/https://doi.org/10.1029/2024JD040732, 2024.

Karpowicz, B. M., Stegmann, P. G., Johnson, B. T., Christophersen, H. W., Hyer, E. J., Lambert, A., and Simon, E.: pyCRTM: A python interface for the community radiative transfer model, Journal of Quantitative Spectroscopy and Radiative Transfer, 288, 108 263, https://doi.org/https://doi.org/10.1016/j.jqsrt.2022.108263, 2022.

Larosa, S., Cimini, D., Gallucci, D., Nilo, S. T., and Romano, F.: PyRTlib: an educational Python-based library for non-scattering atmospheric microwave radiative transfer computations, Geoscientific Model Development, 17, 2053–2076, https://doi.org/10.5194/gmd-17-2053-2024, 2024.

Leuenberger, D., Haefele, A., Omanovic, N., Fengler, M., Martucci, G., Calpini, B., Fuhrer, O., and Rossa, A.: Improving High-Impact Numerical Weather Prediction with Lidar and Drone Observations, Bulletin of the American Meteorological Society, 101, E1036 – E1051, https://doi.org/10.1175/BAMS-D-19-0119.1, 2020.

Li, J. and Fu, Q.: Absorption Approximation with Scattering Effect for Infrared Radiation, Journal of the Atmospheric Sciences, 57, 2905–2914, https://doi.org/10.1175/1520-0469(2000)057<2905:AAWSEF>2.0.CO;2, 2000.

Liebe, H. J.: An updated model for millimeter wave propagation in moist air, Radio Science, 20, 1069–1089, https://doi.org/https://doi.org/10.1029/RS020i005p01069, 1985.

Liebe, H. J.: MPM—An atmospheric millimeter-wave propagation model, International Journal of Infrared and Millimeter Waves, 10, 631–650, https://doi.org/https://doi.org/10.1007/BF01009565, 1989.

Liebe, H. J., Rosenkranz, P. W., and Hufford, G.: Atmospheric 60-GHz oxygen spectrum: New laboratory measurements and line parameters, Journal of quantitative spectroscopy and radiative transfer, 48, 629–643, 1992.

Liebe, H. J., Hufford, G. A., and Cotton, M.: Propagation modeling of moist air and suspended water/ice particles at frequencies below 1000 GHz, In AGARD, 1993.

Lin, H.-C., Sun, J., Weckwerth, T. M., Joseph, E., and Kay, J.: Assimilation of New York State Mesonet Surface and Profiler Data for the 21 June 2021 Convective Event, Monthly Weather Review, 151, 485 – 507, https://doi.org/10.1175/MWR-D-22-0136.1, 2023.

Liou, K.: Radiation and Cloud Processes in the Atmosphere: Theory, Observation and Modeling, Oxford University, ISBN 9780195049107, 1992.

Martinet, P., Dabas, A., Donier, J.-M., Douffet, T., Garrouste, O., and Guillit, R.: 1D-Var temperature retrievals from microwave radiometer and convective scale model, Tellus A: Dynamic Meteorology and Oceanography, 67, 27 925, https://doi.org/10.3402/tellusa.v67.27925, 2015.

Martinet, P., Cimini, D., Burnet, F., Ménétrier, B., Michel, Y., and Unger, V.: Improvement of numerical weather prediction model analysis during fog conditions through the assimilation of ground-based microwave radiometer observations: a 1D-Var study, Atmospheric Measurement Techniques, 13, 6593–6611, https://doi.org/10.5194/amt-13-6593-2020, 2020.

Matricardi, M., Chevallier, F., Kelly, G., and Thépaut, J.-N.: An improved general fast radiative transfer model for the assimilation of radiance observations, Quarterly Journal of the Royal Meteorological Society, 130, 153–173, https://doi.org/https://doi.org/10.1256/qj.02.181, 2004.

McMillin, L. M., Crone, L. J., and Kleespies, T. J.: Atmospheric transmittance of an absorbing gas. 5. Improvements to the OPTRAN approach, Applied optics, 34, 8396–8399, https://doi.org/10.1364/AO.34.008396, 1995.

Mlawer, E. J., Payne, V. H., Moncet, J.-L., Delamere, J. S., Alvarado, M. J., and Tobin, D. C.: Development and recent evaluation of the MT_CKD model of continuum absorption, Philosophical Transactions of the Royal Society A: Mathematical, Physical and Engineering Sciences, 370, 2520–2556, 2012.

Moradi, I., Goldberg, M., Brath, M., Ferraro, R., Buehler, S. A., Saunders, R., and Sun, N.: Performance of Radiative Transfer Models in the Microwave Region, Journal of Geophysical Research: Atmospheres, 125, e2019JD031 831, https://doi.org/https://doi.org/10.1029/2019JD031831, 2020.

Rochon, Y. J., Garand, L., Turner, D. S., and Polavarapu, S.: Jacobian mapping between vertical coordinate systems in data assimilation, Quarterly Journal of the Royal Meteorological Society, 133, 1547–1558, https://doi.org/https://doi.org/10.1002/qj.117, 2007.

Rosenkranz, P.: Line-by-line microwave radiative transfer (non-scattering), https://doi.org/10.21982/M81013, 2017.

Rosenkranz, P. W.: Water vapor microwave continuum absorption: A comparison of measurements and models, Radio Science, 33, 919–928, https://doi.org/https://doi.org/10.1029/98RS01182, 1998.

Saunders, R., Matricardi, M., and Brunel, P.: An improved fast radiative transfer model for assimilation of satellite radiance observations, Quarterly Journal of the Royal Meteorological Society, 125, 1407–1425, https://doi.org/https://doi.org/10.1002/qj.1999.49712555615, 1999.

Saunders, R., Hocking, J., Turner, E., Rayer, P., Rundle, D., Brunel, P., Vidot, J., Roquet, P., Matricardi, M., Geer, A., Bormann, N., and Lupu, C.: An update on the RTTOV fast radiative transfer model (currently at version 12), Geoscientific Model Development, 11, 2717–2737, https://doi.org/10.5194/gmd-11-2717-2018, 2018.

Stegmann, P. G., Johnson, B., Moradi, I., Karpowicz, B., and McCarty, W.: A deep learning approach to fast radiative transfer, Journal of Quantitative Spectroscopy and Radiative Transfer, 280, 108 088, https://doi.org/https://doi.org/10.1016/j.jqsrt.2022.108088, 2022.

Toon, O. B., McKay, C. P., Ackerman, T. P., and Santhanam, K.: Rapid calculation of radiative heating rates and photodissociation rates in inhomogeneous multiple scattering atmospheres, Journal of Geophysical Research: Atmospheres, 94, 16 287–16 301, https://doi.org/10.1029/JD094iD13p16287, 1989.

Turner, D. D., Clough, S. A., Liljegren, J. C., Clothiaux, E. E., Cady-Pereira, K. E., and Gaustad, K. L.: Retrieving Liquid Water Path and Precipitable Water Vapor From the Atmospheric Radiation Measurement (ARM) Microwave Radiometers, IEEE Transactions on Geoscience and Remote Sensing, 45, 3680–3690, https://doi.org/10.1109/TGRS.2007.903703, 2007.

Turner, E., Rayer, P., and Saunders, R.: AMSUTRAN: A microwave transmittance code for satellite remote sensing, Journal of Quantitative Spectroscopy and Radiative Transfer, 227, 117 – 129, https://doi.org/https://doi.org/10.1016/j.jqsrt.2019.02.013, 2019.

Vural, J., Merker, C., Löffler, M., Leuenberger, D., Schraff, C., Stiller, O., Schomburg, A., Knist, C., Haefele, A., and Hervo, M.: Improving the representation of the atmospheric boundary layer by direct assimilation of ground-based microwave radiometer observations, Quarterly Journal of the Royal Meteorological Society, 150, 1012–1028, https://doi.org/https://doi.org/10.1002/qj.4634, 2024.

Wei, J., Shi, Y., Ren, Y., Li, Q., Qiao, Z., Cao, J., Ayantobo, O. O., Yin, J., and Wang, G.: Application of Ground-Based Microwave Radiometer in Retrieving Meteorological Characteristics of Tibet Plateau, Remote Sensing, 13, https://doi.org/10.3390/rs13132527, 2021.

Wei, Y., Peng, K., Ma, Y., Sun, Y., Zhao, D., Ren, X., Yang, S., Ahmad, M., Pan, X., Wang, Z., and Xin, J.: Validation of ERA5 Boundary Layer Meteorological Variables by Remote-Sensing Measurements in the Southeast China Mountains, Remote Sensing, 16, https://doi.org/10.3390/rs16030548, 2024.

Weng, F. and Liu, Q.: Satellite Data Assimilation in Numerical Weather Prediction Models. Part I: Forward Radiative Transfer and Jacobian Modeling in Cloudy Atmospheres, Journal of the Atmospheric Sciences, 60, 2633 – 2646, https://doi.org/10.1175/1520-0469(2003)060<2633:SDAINW>2.0.CO;2, 2003.

Weng, F., Yu, X., Duan, Y., Yang, J., and Wang, J.: Advanced Radiative transfer Modeling System (ARMS): A New-Generation Satellite Observation Operator Developed for Numerical Weather Prediction and Remote Sensing Applications, Advances in Atmospheric Sciences, 37, 131–136, https://doi.org/https://doi.org/10.1007/s00376-019-9170-2, 2020.

Wu, J., Guo, J., Yun, Y., Yang, R., Guo, X., Meng, D., Sun, Y., Zhang, Z., Xu, H., and Chen, T.: Can ERA5 reanalysis data characterize the pre-storm environment?, Atmospheric Research, 297, 107 108, https://doi.org/https://doi.org/10.1016/j.atmosres.2023.107108, 2024.

Yang, J. and Min, Q.: Retrieval of Atmospheric Profiles in the New York State Mesonet Using One-Dimensional Variational Algorithm, Journal of Geophysical Research: Atmospheres, 123, 7563–7575, https://doi.org/https://doi.org/10.1029/2018JD028272, 2018.

Yang, J., Ding, S., Dong, P., Bi, L., and Yi, B.: Advanced Radiative transfer Modeling System developed for satellite data assimilation and remote sensing applications, Journal of Quantitative Spectroscopy and Radiative Transfer, 251, 107 043, https://doi.org/https://doi.org/10.1016/j.jqsrt.2020.107043, 2020.

Zhang, F., Wu, K., Li, J., Yang, Q., Zhao, J.-Q., and Li, J.: Analytical Infrared Delta-Four-Stream Adding Method from Invariance Principle, Journal of the Atmospheric Sciences, 73, 4171–4188, https://doi.org/10.1175/JAS-D-15-0317.1, 2016.

Zhang, F., Shi, Y.-N., Li, J., Wu, K., and Iwabuchi, H.: Variational Iteration Method for Infrared Radiative Transfer in a Scattering Medium, Journal of the Atmospheric Sciences, 74, 419–430, https://doi.org/10.1175/JAS-D-16-0172.1, 2017.

Zhang, F., Wu, K., Li, J., Zhang, H., and Hu, S.: Radiative transfer in the region with solar and infrared spectra overlap, Journal of Quantitative Spectroscopy and Radiative Transfer, 219, 366 – 378, https://doi.org/https://doi.org/10.1016/j.jqsrt.2018.08.025, 2018.